The Astrophysical Journal, 972:180 (19pp), 2024 September 10 https://doi.org/10.3847/1538-4357/ad55f0

Kinematics and Metallicity of the Dwarf Spheroidal Galaxy Andromeda XVIII

Kateryna A. Kvasova[1], Evan N. Kirby[1], and Rachael L. Beaton[2]
[1] Department of Physics and Astronomy, University of Notre Dame, 225 Nieuwland Science Hall, Notre Dame, IN 46556, USA; kkvasova@nd.edu
[2] Space Telescope Science Institute, 3700 San Martin Drive, Baltimore, MD 21218, USA
Received 2024 April 16; revised 2024 May 31; accepted 2024 June 4; published 2024 September 5

Abstract

Andromeda XVIII is an isolated dwarf galaxy 579 kpc away from the nearest large galaxy, M31. It is a candidate "backsplash galaxy" that might have been affected by a close passage to M31. We present new Keck/DEIMOS spectroscopy of Andromeda XVIII to assess the likelihood that it is a backsplash galaxy. We estimated the velocities, metallicities ([Fe/H]), and α-enhancements ([α/Fe]) for 56 probable members. Based on the abundances of 38 stars with low errors (δ[Fe/H] < 0.3), parameters for the simplest chemical evolution models were estimated using the maximum likelihood coupled with a Markov Chain Monte Carlo (MCMC) method. The metallicity distribution is inconsistent with these models, due to a sharp metal-rich cutoff. We estimated Andromeda XVIII's mean heliocentric velocity, rotation velocity, position angle of the rotation axis, and velocity dispersion using the maximum likelihood coupled with an MCMC. There is no evidence for bulk rotation, though subpopulations might be rotating. The mean heliocentric velocity is $-337.2\,\mathrm{km\,s^{-1}}$, such that the line-of-sight velocity relative to M31 is lower than the escape velocity from M31. Together, the metallicity distribution and the mean velocity are consistent with a sudden interruption of star formation. For possible causes of this quenching, we considered gas loss due to ram pressure stripping during a close passage by M31 or due to a past major merger. However, we cannot rule out internal feedback (i.e., a terminal wind).

Unified Astronomy Thesaurus concepts: Dwarf galaxies (416); Local Group (929); Galaxy chemical evolution (580); Stellar abundances (1577)

Materials only available in the online version of record: machine-readable table

1. Introduction

The Milky Way (MW) and Andromeda (M31) are the two dominant galaxies in the Local Group. However, they are dominant only in luminosity and mass. By number, there are far more dwarf galaxies in the Local Group. Some of them are satellites of the MW or M31, and others are isolated. The MW has over 60 known satellites, and M31 has over 30. The Local Group hosts about 15 more isolated dwarf galaxies.[3]

Any differences between the MW and M31 satellite populations seem insignificant when satellite dwarf galaxies are compared to isolated dwarf galaxies. Most obviously, the vast majority of satellite galaxies have no gas, and the vast majority of isolated galaxies have lots of gas (Spekkens et al. 2014), with typical gas-to-stellar mass ratios around 1. Isolated galaxies are also more likely to obey the radius–luminosity relation (Higgs & McConnachie 2021) and the metallicity–luminosity relation (Kirby et al. 2013). Altogether, the evidence suggests that dwarf galaxies experience a dramatic transition when they enter the sphere of influence of a large host, like the MW or M31. Their morphologies transition from dwarf irregular (dIrr) to dwarf spheroidal (dSph), and they lose their gas from ram pressure stripping. Galaxies with close enough pericentric passages can even lose dark matter and stellar mass to tidal stripping.

One intriguing class of isolated dwarf galaxies is the isolated dSphs. There are three famous isolated dSphs: Cetus, Tucana, and Andromeda XVIII (And XVIII). The prevalence of gas-rich isolated dwarf galaxies has led to the concept of "backsplash galaxies" (Teyssier et al. 2012). The orbits of backsplash galaxies once passed within the virial radius of a large galaxy, like the MW, even if those orbits are unbound. The brief interaction could be enough for ram pressure stripping to remove gas, quench star formation, and morphologically transform the galaxy from dIrr to dSph. The backsplash mechanism could be the proximate cause of the formation of supposedly dark-matter-free, ultra-diffuse dwarf galaxies (Danieli et al. 2019; Benavides et al. 2021). Therefore, it is important to study the backsplash mechanism and its exemplars.

And XVIII is a particularly interesting subject for further study. McConnachie et al. (2008) discovered and characterized And XVIII from CFHT/MegaPrime imaging. However, a large portion of the galaxy was hidden by a CCD chip gap. They found that the tip of the red giant branch (TRGB) has a magnitude $I_0 = 21.6$. Makarova et al. (2017) later found a TRGB magnitude of F814W = 21.7 from HST/ACS photometry. Tollerud et al. (2012) obtained the first spectra of stars in And XVIII.

It is not likely to be a backsplash galaxy of the MW, because its Galactocentric distance is about 1.33 Mpc. On the other hand, its three-dimensional distance from M31 is only 579 kpc (Makarova et al. 2017). Therefore, it could be an example of an M31 backsplash dwarf galaxy. Its photometrically measured star formation history (SFH) shows two epochs of intense star formation: one 12–14 Gyr ago, and another that started about

[3] These numbers are subject to heavy observational bias, where it is easier to detect satellites of the MW compared to more distant dwarf galaxies. See Drlica-Wagner et al. (2020) for an estimate of the luminosity function of MW satellites, corrected for selection bias.

8 Gyr ago, with a sudden cessation about 1.5 Gyr ago (Makarova et al. 2017). The second star formation period might be associated with a flyby of M31.

The purpose of this work is to determine the features of the evolution of And XVIII using accurate measurements of kinematical properties, metallicities, and α-enhancement of the most probable And XVIII members, together with chemical evolution models. Specifically, we determine here the role of gas loss—ram pressure stripping—based on chemical properties, but also the presence or absence of rotation and the line-of-sight dwarf galaxy's velocity relative to M31, to find whether it can exclude the possibility of And XVIII being a backsplash dwarf.

2. Observations

We observed And XVIII with the Deep Imaging Multi-Object Spectrograph (DEIMOS; Faber et al. 2003) on the Keck II telescope on 2022 September 19–22. We designed two slitmasks: and18a and and18b. The total exposure times were 590 and 556 minutes, respectively, for and18a and and18b. The conditions were excellent, with seeing ranging between 0.″5 and 0.″8. The paragraphs below describe the target selection.

Each slitmask has an approximate sky projection of $16' \times 5'$. We used the OG550 order-blocking filter with the 1200G grating at a central wavelength of 7800 Å. The slit widths were 0.″8, resulting in a spectral resolving power of $R \sim 6000$, or a line width of 1.3 Å FWHM. We used the `spec2d` pipeline from the DEEP2 Galaxy Redshift Survey (Cooper et al. 2012; Newman et al. 2013) to reduce the raw frames. The result of the pipeline is a list of one-dimensional, sky-subtracted, wavelength-calibrated spectra. We used some improvements to the wavelength calibration and one-dimensional object extraction described by Kirby et al. (2015a, 2015b).

We selected targets from three different catalogs. First, we selected stars from photometry acquired with the Hubble Space Telescope Advanced Camera for Surveys (SNAP project 13442, PI: R. B. Tully; Makarova et al. 2017). And XVIII was observed with the F606W and F814W filters. L. Makarova kindly shared with us the photometric catalog, which was the output of DOLPHOT (Dolphin 2016). The catalog had pixel positions, which we converted to sky coordinates using the world coordinate solution of the FITS files of the observations available from the MAST archive.

The ACS field of view is significantly smaller than a DEIMOS slitmask. Therefore, we also included photometry from the Pan–Andromeda Archaeological Survey (PAndAS; Ibata et al. 2014; McConnachie et al. 2018). PAndAS is a wide-field survey of M31 and M33 with CFHT/MegaCam in the g and i filters. The survey has gaps between CCDs. Unfortunately, one of these gaps coincided with the center of And XVIII. Therefore, PAndAS photometry is useful only for stars in the outer regions of the dwarf galaxy.

Photometry from the Spectroscopic and Photometric Landscape of the Andromeda Stellar Halo (SPLASH) project was also used. The imaging was obtained on the MOSAIC 1.1 instrument on the Kitt Peak National Observatory (KPNO) Mayall 4 m telescope using the Washington filter system (M, T_2; Canterna 1976) supplemented with the *DDO*51 filter that is sensitive to stellar surface gravity for late-type stars (Majewski et al. 2000) (NOIRLab Prop. ID 2010B-0596; PI: R. Beaton). MOSAIC had a field of view of $36' \times 36'$ using eight $2k \times 4k$ CCDs with chip gaps. And XVIII was placed on a single CCD for uninterrupted coverage of the dwarf galaxy. Image processing used the `mscred` package in IRAF (a detailed description is given in Beaton 2014). The photometry was obtained using the DAOPHOT family of programs (Stetson 1987, 1990, 1994) following the procedures used for the broader SPLASH survey (Beaton 2014; Ostheimer & Craig 2003) and used other SPLASH spectroscopic follow-up (e.g., Majewski et al. 2007; Tollerud et al. 2012). The photometry was calibrated directly to Landolt standards (Geisler 1996; Landolt 1992), or for data taken in non-photometric conditions, bootstrapped to observations on photometric nights. Image astrometry used USNO-B (Monet et al. 2003). We converted M and T_2 magnitudes to the Johnson–Cousins system based on the transformations of Majewski et al. (2000, their Section 2.2).

We supplemented the above catalogs with photometry from the Gaia DR3 catalog. The Gaia catalog contains very few And XVIII members, because they are too faint. Nonetheless, the catalog is still useful for slitmask alignment stars.

We matched stars from the different catalogs based on their coordinates. Then, we assigned priorities for placement on the slitmasks to the stars based on their position in the color–magnitude diagram (CMD), and in some cases, from the color–color diagram involving the Washington *DDO*51 filter. We drew a generous selection polygon in the three CMDs defined by the HST/ACS, PAndAS/CFHT, and KPNO (transformed to Johnson–Cousins) filter sets. Stars outside of the polygons were considered nonmembers. Within the selection boxes, the stars were prioritized by magnitude. First, stars with brighter HST/ACS F814W magnitudes were given higher priority. Then, for stars not observed with HST, stars with brighter CFHT magnitudes were given higher priority. Finally, for stars observed with neither HST nor CFHT, stars with brighter KPNO magnitudes were given higher priority.

The *DDO*51 filter brackets the Mg b triplet, which is sensitive to surface gravity (Majewski et al. 2000). Dwarf stars have strong Mg b triplet features and are therefore fainter in the *DDO*51 filter relative to giant stars of the same M–$T2$ color (as a proxy for temperature). Washington color–color diagrams, specifically M–$T2$ versus M–*DDO*51 (see, e.g., Majewski et al. 2000; Tollerud et al. 2012), can separate foreground dwarf stars in the Milky Way from target giants in the M31 system (including And XVIII). The strength of the Mg b triplet varies with stellar temperature, and dwarf stars in the Milky Way fall on a characteristic "swoosh" shape in the color–color diagram (see Majewski et al. 2000, their Figure 6). The giant probability, or gprob, (Ostheimer & Craig 2003) is the fraction of a source's color–color error circle within the region populated by giants (for an example, see Figure 2 of Tollerud et al. (2012)). Following other SPLASH methodologies, we considered stars with gprob < 0.1 as nonmembers. They were given priorities as low as stars that fell outside of the CMD selection polygons.

We created the slitmask designs with the `dsimulator` software. Figure 1 shows the slitmasks projected onto the sky. Figure 2 shows the stars' color–magnitude diagrams in the filter sets of the various source catalogs.

3. Methods

We measured radial velocities (Section 3.2) and abundances (Section 3.3) from the DEIMOS spectra. In order to make these measurements, the spectra needed to be prepared for analysis (Section 3.1).

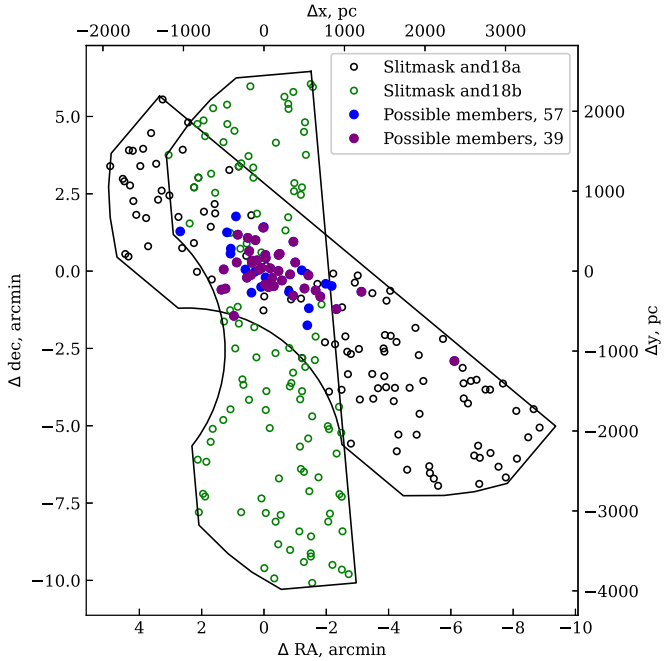

Figure 1. Positions of objects observed via DEIMOS slitmasks and18a and and18b with surrounding objects. The probable members of And XVIII are shown in blue and purple (57 and 39 stars, respectively, including the metal-rich star PAndAS9654; see Section 4.1).

3.1. Preparation of Spectra

We divided each spectrum by a telluric standard spectrum following the procedure of Kirby et al. (2008, their Section 3.2). The standard star was HR7346, a rapidly rotating star of spectral type B9V. The star was observed on 2015 May 19 by drifting the star across a 0.″7 slit during the exposure.

The spectrum was continuum-normalized. The absorption depths were scaled to the airmass of the And XVIII observations before division.

Still, some wavelength windows are severely disturbed by telluric absorption, and we excluded them from the measurements of radial velocity and elemental abundances (Kirby et al. 2008). However, these regions are still included in the slit miscentering correction described in Section 3.2.

3.2. Radial Velocities

We measured radial velocities by cross-correlating each spectrum with a suite of template spectra. Kirby et al. (2015a) described the observations of the template spectra, as well as the procedure for performing the cross-correlation, which was based on the work of Simon & Geha (2007). The uncertainties in radial velocity were estimated from Monte Carlo resampling of the spectra. The redshift corresponding to this radial velocity, $z_{\rm rest}$, is used to place the spectra in the rest frame.

The velocities include a correction for slit miscentering, which can shift the zero point of a spectrum's wavelength by up to $\sim$20 km s^{-1}. This correction is not necessary to shift the spectra into the rest frame, but it is necessary to measure absolute velocities with respect to a standard of rest. We followed the procedure of Sohn et al. (2007), which is further expanded upon by Kirby et al. (2015a). In summary, the telluric A and B bands are cross-correlated with the same spectral region in the telluric standard star. To compute the stellar velocities in the geocentric frame, the inferred "redshift" of the telluric features is added to the observed redshift of the star.

We shifted the velocities to the heliocentric reference frame based on the star's coordinates and mean observation time. The heliocentric velocity for a star is called $v_{\rm helio}$. We use these velocities in a procedure to infer the kinematic properties of And XVIII in Section 3.5, with the results presented in Section 4.2.

3.3. Elemental Abundances

Our approach is based on that of Kirby et al. (2008, 2009, 2010) and Escala et al. (2019). We derived the effective temperature $T_{\rm eff}$, surface gravity $\log g$, metallicity [Fe/H], and α-enhancement [α/Fe] via spectral synthesis. We measured an averaged α abundance, but we did not measure individual α element abundances. An alternative approach with low- to medium-resolution spectroscopy is an empirical relation between abundance and line strengths, such as the Ca II triplet. However, those relations possibly confuse the abundances of different elements. For example, Ca II triplet strength could depend on both the Ca and Fe abundances, where Fe abundance is a proxy for free electron fraction and therefore the overall metallicity (Battaglia et al. 2008; Starkenburg et al. 2010). Strong lines like the Ca II triplet are poorly modeled in local thermodynamic equilibrium (LTE). Our spectral synthesis approach assumes LTE, so we exclude such lines. Kirby et al. (2008, 2009, 2010) list the rest-frame spectral regions considered within our analysis.

In summary, we measured the aforementioned four stellar parameters by matching the observed spectra to a grid of synthetic spectra generated using the LTE spectral synthesis code MOOG (Sneden 1973; Sneden et al. 2012). This approach is especially useful for spectra of distant stars—such as those in And XVIII–whose spectra have low S/N. Although individual lines may be only poorly detected, the ensemble of many lines has enough signal to permit measurements of [Fe/H] and [α/Fe]. The spectra were synthesized in model atmospheres generated with ATLAS9 (Kurucz 2017). The grid of atmospheres and spectra models is described by Kirby (2011).

In order to make optimal use of all available data, we used broadband photometric magnitudes and colors to estimate $T_{\rm eff}$ and $\log g$. We interpolated a model isochrone using the known color and magnitude of each star, combined with the distance modulus of And XVIII ($(m-M)_0 = 25.62$; Makarova et al. 2017). PARSEC isochrones[4] (Girardi et al. 2002) were used for all three photometric systems of observed objects: Johnson–Cousins (KPNO), CFHT (PAndAS), and HST WFC (ACS). We assumed an age of 12 Gyr. The values of $T_{\rm eff}$ and $\log g$ are not very sensitive to the choice of isochrone age.

With $T_{\rm eff}$ and $\log g$ fixed to their photometric values, we used χ^2 minimization to fit each observed spectrum to the interpolated grid of synthetic spectra. For continuum normalization during the fit, we used third-order B spline interpolation. We began with an initial continuum that was iteratively refined for specific regions of spectra (Kirby et al. 2008). The breakpoint spacing was chosen to be 100 pixels in order to avoid overfitting. We used 5σ and 3σ clipping for the initial and refined continua, respectively. The best-fitting values

[4] The isochrones for all three photometric systems were generated using the software CMD 3.7: http://stev.oapd.inaf.it/cgi-bin/cmd.

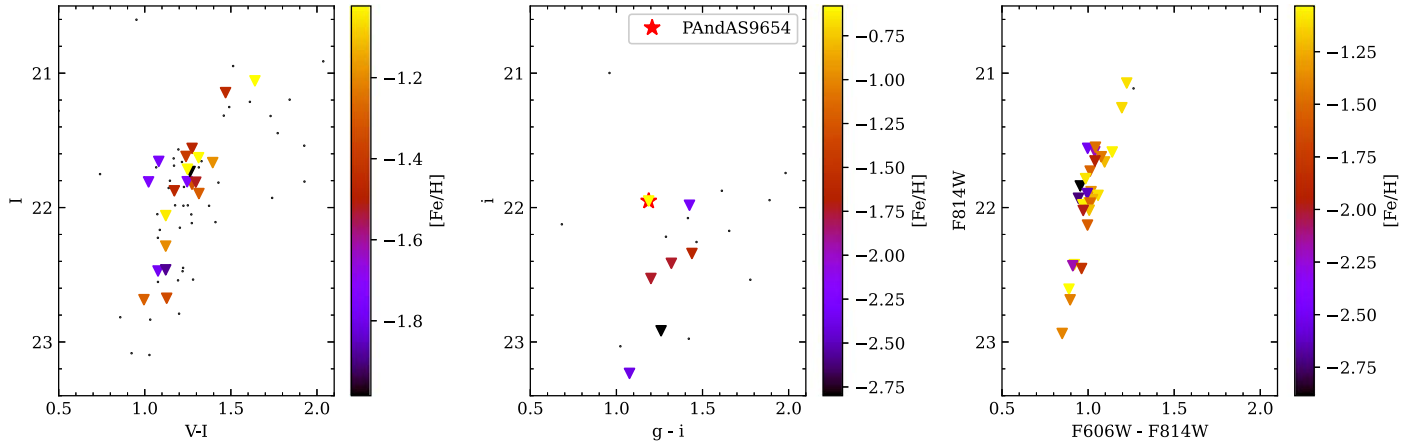

Figure 2. Color–magnitude diagrams (CMD) for 56 probable And XVIII members plus PAndAS9654, assumed to be an M31 halo star (see Section 4.1), in three photometric systems: KPNO (left), PAndAS (middle), and HST/ACS (right). The color gradient shows the [Fe/H] values for the stars. Although PAndAS9654 is on the left side of the CMD in the middle panel, its spectroscopic metallicity is the largest in our sample. According to Figure 6, this star is also α-enhanced compared to the other 56 objects.

of [Fe/H] and [α/Fe] comprise our measurements of those parameters for each star.

[α/Fe] abundances were calculated from a simultaneous fit to Mg, Si, Ca, and Ti wavelength masks, following the procedure of Kirby et al. (2008). We do not report abundances of individual α elements. Generally low S/N (e.g., more than half of estimated members have S/N < 15) would result in large errors for these individual abundances.

Table 1 gives object names, slitmasks, S/N, heliocentric velocities, coordinates (ICRS), membership, and also $T_{\rm eff}$, surface gravity, [Fe/H], [α/Fe], and random errors for some of the stars that we observed. The table contains only stars with $v_{\rm helio} < 100\,{\rm km\,s^{-1}}$ and $v_{\rm helio} > -400\,{\rm km\,s^{-1}}$ (in total 166 objects). Nonmembers are at different observed velocities than And XVIII, while the isochrone method for $T_{\rm eff}$ and surface gravity was used with the same distance modulus, which caused us to classify PAndAS9654 as an M31 halo star, not a member of And XVIII (Figure 2).

Although most stars have measured abundances, only those with δ[Fe/H] < 1 are included in Table 1. For membership criteria, see Section 4.1.

3.4. Analytic Chemical Evolution Models

The measured metallicity distribution ($N_{\rm stars}$ in bins of [Fe/H]) of a galaxy can be described by chemical evolution models. These models are used for a general assessment of the details of star formation, interaction with the environment, and the ratio of the mass of gas to the mass of stars. The Leaky Box, Pre-Enriched, Accretion, and Ram Pressure Stripping models (Kirby et al. 2013 and references therein) were used in this work (see Table 2). All of them are one-zone models, and they share simple assumptions, including instantaneous recycling of material and the Kennicutt–Schmidt law for the star formation rate.

3.4.1. Leaky Box Model

The Leaky Box model assumes that all stars in the galaxy form from gas with a primordial composition. The galaxy is subject to gas loss ("leaking") due to internal feedback. This also can be called the Pristine model. Its metallicity distribution is described by the formula

$$\frac{dN}{d[{\rm Fe/H}]} \propto \left(\frac{10^{[{\rm Fe/H}]}}{p_{\rm eff}}\right)\exp\left(\frac{-10^{[{\rm Fe/H}]}}{p_{\rm eff}}\right), \quad (1)$$

where $p_{\rm eff}$ is the effective yield. The effective yield is $p_{\rm eff} = p/(1+\eta)$, where the true yield $p = Z/(\ln(\mu^{-1}))$ is in units of the solar metal fraction ($Z_\odot$). η is the mass loading factor, or the proportionality coefficient between outflow and star formation rate (SFR); Z is the current gas-phase metallicity; and μ is the current gas fraction.

3.4.2. Pre-Enriched Model

The Pre-Enriched model assumes an enriched composition of the initial gas. Its metallicity distribution is described by

$$\frac{dN}{d[{\rm Fe/H}]} \propto \left(\frac{10^{[{\rm Fe/H}]} - 10^{[{\rm Fe/H}]_0}}{p_{\rm eff}}\right) \times \exp\left(\frac{-10^{[{\rm Fe/H}]}}{p_{\rm eff}}\right). \quad (2)$$

$[{\rm Fe/H}]_0$ describes the initial galaxy's gas metallicity. For very low values ($[{\rm Fe/H}]_0 \lesssim -5$), the Pre-Enriched model reduces to the Leaky Box model.

3.4.3. Accretion Model

The Accretion model contains three parameters: the effective yield $p_{\rm eff}$, the ratio of the final mass to the initial (gas) mass M, and the stellar mass fraction s, which is determined from the numerical solution of the following equation:

$$[{\rm Fe/H}](s) = \log\left[p_{\rm eff}\left(\frac{M}{1+s-s/M}\right)^2 \times \left(\ln\left(\frac{1}{1-s/M}\right) - \frac{s}{M}\left(1-\frac{1}{M}\right)\right)\right] \quad (3)$$

Table 1
Catalog of Velocities and Metallicities

Name	Slitmask	S/N $\mathring{A}^{-1}$	v_{helio} (km s^{-1})	δv_{helio} (km s^{-1})	T_{eff} (K)	δT_{eff} (K)	log(g) (cm s^{-2})	[Fe/H]	δ[Fe/H]	[α/Fe]	δ[α/Fe]	Member	R.A. (h)	(min)	(s)	Decl. (deg)	(arcmin)	(arcsec)
PAndAS2422	and18b	27.27	−50.16	0.84	3848.25	0.0056	0.27	−3.0	0.071	1.2	0.067	N	00	02	14.06	+44	55	43.8
PAndAS2476	and18b	27.59	6.93	1.19	3772.0	0.0051	0.23	−2.684	0.064	1.125	0.072	N	00	02	01.71	+44	55	50.1
PAndAS2665	and18b	30.46	−110.05	22.49	…	…	…	…	…	…	…	N	00	02	05.63	+44	56	06.3
PAndAS3420	and18b	23.77	−156.47	3.06	3644.22	0.005	0.18	−3.245	0.131	1.2	0.115	N	00	02	12.07	+44	57	13.9
PAndAS3620	and18b	24.12	−11.58	1.43	3500.0	0.0051	0.08	−3.256	0.112	1.2	0.093	N	00	02	13.86	+44	57	30.7
PAndAS4128	and18b	4.77	−89.13	19.91	…	…	…	…	…	…	…	N	00	02	00.52	+44	58	07.3
PAndAS4556	and18b	8.79	−17.69	40.98	…	…	…	…	…	…	…	N	00	02	11.52	+44	58	37.8
PAndAS5740	and18b	18.71	−35.9	2.15	3552.6	0.0048	0.26	−2.436	0.127	0.53	0.167	N	00	02	00.25	+45	00	06.3
PAndAS5837	and18b	14.23	−91.43	3.74	…	…	…	…	…	…	…	N	00	02	02.48	+45	00	13.4
PAndAS5861	and18b	24.67	−4.82	1.47	3500.0	0.0051	0.08	−3.528	0.174	1.2	0.132	N	00	02	13.25	+45	00	15.5

Note. This table is available in its entirety in machine-readable form.

(This table is available in its entirety in machine-readable form in the online article.)

Table 2
Adopted and Derived[a] Parameters of And XVIII

Property	39 stars[b] (57)	38 stars, (56)	38 stars, [α/H]	Priors	Units
R.A. center		$0.560417^{+0.00940}_{-0.00940}$			degrees
Decl. center		$45.08889^{+0.00193}_{-0.00193}$			degrees
Distance		$1.33^{+0.88}_{-0.88}$			Mpc
		Chemical Evolution Models			
$p_{\rm eff}$ (Leaky Box)	$5.4^{+1.0}_{-0.8}$	$4.9^{+1.0}_{-0.8}$	$7.6^{+1.6}_{-1.2}$	0.0 – 100.0	10^{-2}*$Z_\odot$
$p_{\rm eff}$ (Pre-Enriched)	$5.0^{+1.0}_{-0.8}$	$4.5^{+0.9}_{-0.8}$	$5.3^{+1.4}_{-1.1}$	1.0 – 25.0	10^{-2}*$Z_\odot$
[Fe/H]$_0$ (Pre-Enriched)	$-3.20^{+0.55}_{-1.62}$	$-3.03^{+0.44}_{-1.53}$	$-2.04^{+0.19}_{-0.31}$	−5.0 – 0.5	
$p_{\rm eff}$ (Ram PS)	$0.13^{+0.25}_{-0.08}$	$0.24^{+0.15}_{-0.12}$	$0.17^{+0.19}_{-0.09}$	0.0 – 0.5	$Z_\odot$
$z_{\rm str}$ (Ram PS)	$0.17^{+0.79}_{-0.09}$	$0.11^{+0.03}_{-0.04}$	$0.21^{+0.59}_{-0.14}$	$1.52^{*}10^{-3}$ – 1.52	10^{-2}
$\zeta_{\rm str}$ (Ram PS)	$3.4^{+2.3}_{-2.0}$	$4.6^{+1.6}_{-2.0}$	$1.1^{+0.6}_{-0.7}$	0.0 – 7.0	
$p_{\rm eff}$ (Accretion)	$5.4^{+0.7}_{-0.7}$	$4.7^{+0.7}_{-0.5}$	$7.2^{+0.9}_{-0.9}$	0.0 – 50.0	10^{-2}*$Z_\odot$
$M_{\rm Acc}$ (Accretion)	$3.5^{+2.1}_{-1.3}$	$3.4^{+2.2}_{-1.2}$	$6.9^{+2.1}_{-2.9}$	1.0 – 10.0	
		Kinematic Models			
$\langle v_{\rm helio}\rangle$ (no rotation)	$-337.3^{+1.4}_{-1.3}$	$-337.2^{+1.5}_{-1.4}$		trial run	km s^{-1}
σ_v (no rotation)	$9.8^{+1.1}_{-0.9}$	$10.0^{+1.1}_{-1.0}$		trial run	km s^{-1}
$\langle v_{\rm helio}\rangle$ (with rotation)	$-337.3^{+1.4}_{-1.4}$	$-337.3^{+1.4}_{-1.4}$		trial run	km s^{-1}
σ_v (with rotation)	$9.9^{+1.1}_{-1.0}$	$10.0^{+1.2}_{-1.0}$		trial run	km s^{-1}
$v_{\rm rot}$	$1.7^{+1.7}_{-1.2}$	$1.8^{+1.7}_{-1.2}$		trial run	km s^{-1}
$\theta_{\rm axis}$	$3.9^{+1.3}_{-1.6}$	$3.9^{+1.3}_{-1.6}$		trial run	rad

Notes.
[a] The center coordinates and the distance were taken from Makarova et al. (2017). The metallicity of the Sun was taken to be 0.0152 (see Girardi et al. 2002). Values were taken from corner plots obtained after 500 (10000) burn-in steps and a thinning parameter of 50 (100) for *emcee* for chemical evolution models (velocity models). Errors cover the 68% confidence interval.
[b] The sample of 56 stars requires membership based on kinematics and the sodium line criterion. The sample of 39 stars further excludes stars with high metallicity errors (δ[Fe/H]<0.3). The next column is for the same members excluding the possible M31 halo star (PAndAS9634). The last column is for chemical evolution models parameters for the [α/H] distribution. Prior edges for ζ and z_s in the RPS model were taken as 0–2 and $z_\odot^{*}10^{-5}$ – $z_\odot$, respectively.

$$\frac{dN}{d\,[\mathrm{Fe/H}]} \propto \left(\frac{10^{[\mathrm{Fe/H}]}}{p_{\rm eff}}\right)\left[1 + s\left(1 - \frac{1}{M}\right)\right] \times \left[\left(1 - \frac{s}{M}\right)^{-1} - 2\left(1 - \frac{1}{M}\right)\left(\frac{10^{[\mathrm{Fe/H}]}}{p_{\rm eff}}\right)\right]^{-1}. \quad (4)$$

3.4.4. Ram Pressure Stripping Model

The Ram Pressure Stripping model describes the evolution of a dwarf galaxy that lost its gas due to a close passage by the host galaxy. The motion of such a galaxy through the comparatively dense CGM of the host galaxy exerts a pressure on the dwarf galaxy that expels its gas. The model depends on three parameters, namely $p_{\rm eff}$, the effective yield; [Fe/H]$_s$, the metallicity of the galaxy at the moment that gas loss commences; and ζ, a parameter that describes the intensity, expressed as a fraction of the ram pressure gas loss in comparison to the gas loss caused by supernova winds (see Kirby et al. 2013):

$$\frac{dN}{d\,[\mathrm{Fe/H}]} \propto \left(\frac{10^{[\mathrm{Fe/H}]}}{p_{\rm eff}}\right)\left[\exp\left(\frac{-10^{[\mathrm{Fe/H}]}}{p_{\rm eff}}\right) + \zeta\left(\exp\left(\frac{10^{[\mathrm{Fe/H}]_s} - 10^{[\mathrm{Fe/H}]}}{p_{\rm eff}}\right) - 1\right)\right]. \quad (5)$$

3.4.5. Likelihood for Chemical Evolution Models

To find the most likely parameters of each model, the likelihood was calculated according to the formula

$$L = \prod_i \int_{-\infty}^{\infty} \frac{dP}{d\,[\mathrm{Fe/H}]} \frac{1}{\sqrt{2\pi}\cdot\delta\,[\mathrm{Fe/H}]_i} \times \exp\left(-\frac{([\mathrm{Fe/H}] - [\mathrm{Fe/H}]_i)^2}{2(\delta\,[\mathrm{Fe/H}]_i)^2}\right) d\,[\mathrm{Fe/H}]. \quad (6)$$

For convenience, the logarithm of L was maximized. The maximization was implemented using the Markov Chain Monte Carlo method of the emcee Python library (Section 3.6).

Each metallicity error includes the systematic error as $\delta\,[\mathrm{Fe/H}]_i = \sqrt{\delta\,[\mathrm{Fe/H}]^2_{i,\rm rand} + 0.106^2}$ (Kirby et al. 2010), where δ[Fe/H]$_{i,\rm rand}$ is the random uncertainty from the spectral fit (Kirby et al. 2015a).

3.5. Kinematics

We assumed a Gaussian distribution of velocities for And XVIII. Although binary stars can inflate the measured velocity dispersion, we ignored them because we do not have multi-epoch spectroscopy. The mean heliocentric velocity and velocity dispersion were estimated using a Markov Chain Monte Carlo (MCMC) method to maximize the likelihood of the galaxy that is described by a normal distribution:

Table 3
MCMC Parameters

Model	N_{par}	N_{walk}	N_{it}	log(L)	AICc	N_{it}	log(L)	AICc	N_{it}	log(L)	AICc
			39 (57) members, [Fe/H]			38 (56) members, [Fe/H]			38 members, [α/H]		
Velocity	2	5	10^5	−212.42	429.06	10^5	−209.23	422.69		–	
Velocity (r.)	4	8	10^6	−211.97	432.71	10^6	−208.78	426.34		–	
Leaky Box	1	10	12000[a]	−316.97	636.04	12000	−306.90	615.91	11800	−307.35	616.81
Pre-Enriched	2	40	12300	−315.56	635.85	11600	−305.19	614.73	15000	−301.89	608.13
Accretion	2	10	4300	−314.32	632.97	4500	−303.80	611.95	4200	−301.76	607.86
RPS	3	30	40900	−316.71	640.11	28000	−300.75	608.20	29700	−307.15	621.00

Notes. The columns show (1) the number of unknown parameters in the model, (2) the number of walkers (chains) in the MCMC, (3) the number of iterations or links in the chain, (4) the maximum logarithm of the likelihood, and (5) the corrected Akaike information criterion (see Sections 3.6 and 4.5).
[a] Leaky Box and Pre-Enriched models were run for 10^4 more iterations.

$$\ln L = -\frac{1}{2}\sum_{i}^{N} \ln\left(2\pi\left((\delta v)_i^2 + \sigma_v^2\right)\right) - \frac{1}{2}\sum_{i}^{N}\left[\frac{\left((v_{\rm helio})_i - \langle v_{\rm helio}\rangle\right)^2}{(\delta v)_i^2 + \sigma_v^2}\right]. \quad (7)$$

We also considered rotation about an axis θ with a separate likelihood function:

$$\ln L = -\frac{1}{2}\sum_{i}^{N} \ln\left(2\pi\left((\delta v)_i^2 + \sigma_v^2\right)\right) - \frac{1}{2}\sum_{i}^{N}\left[\frac{\left((v_{\rm helio})_i - \left(\langle v_{\rm helio}\rangle + v_{\rm rot}\cos(\theta - \theta_i)\right)\right)^2}{(\delta v)_i^2 + \sigma_v^2}\right]. \quad (8)$$

The index of each star is i. The angles are measured with respect to north. Thus, θ_i is the angle between star i and the center of the galaxy. The free parameters are the mean velocity $\langle v_{\rm helio}\rangle$, the velocity dispersion σ_v, the rotation velocity $v_{\rm rot}$, and the position angle of the rotation axis θ. Each star's radial velocity error includes systematic error as $\delta v_i = \sqrt{\delta v_{i,\rm obs}^2 + (1.49\ {\rm km\ s^{-1}})^2}$ (Kirby et al. 2015a).

3.6. MCMC Ensemble Sampler

In this work, we used the MCMC ensemble sampler method to find the most probable parameters of the likelihood functions constructed in Sections 3.4–3.5.

We used the MCMC sampler *emcee*.[5] The mathematical derivation and details of the method are from Goodman & Weare (2010) and Foreman-Mackey et al. (2013). Those authors recommend choosing the number of walkers to be larger than the number of free parameters in the model. The number of parameters, walkers, iterations, log(L), and corrected Akaike information criterion (AICc; Akaike 1974; Sugiura 1978; see Section 4.5) are given in Table 3.

With *emcee*, we measured the mean integrated autocorrelation time every 100 iterations. For the convergence criterion, we required the change of the autocorrelation time relative to the previous measurement to be less than 0.01. The number of links in the chain is not less than 100 times the derived time. Further details on autocorrelation derivation for ensembles of chains are described by Goodman & Weare (2010) and Foreman-Mackey et al. (2013).

[5] https://pypi.org/project/emcee/

4. Results

4.1. Membership

In total, more than 170 objects were observed. However, most of these are nonmembers (some by design) or have spectral quality insufficient for measurement of velocity and/or metallicity.

Only 100 objects have sufficient S/N and quality to measure abundances. Next, 30 objects were excluded due to the presence of strong sodium 8195 Å lines. The lines are used as an indicator of high surface gravity, such as found in foreground dwarf stars (e.g., Gilbert et al. 2006). Figures 4 and 5 show that all of these stars have radial velocity values far from that of And XVIII. After that, 13 objects were excluded based on the velocity criterion: their $v_{\rm helio}$ were more than $3\sigma_v$ away from $\langle v_{\rm helio}\rangle$. Here, we repeated the method used by Kirby et al. (2010). The method consists of iteratively estimating $v_{\rm helio}$ and σ_v. Each iteration considers only objects within $3\sigma_v$ around $\langle v_{\rm helio}\rangle$ (as determined in the previous iteration), until the number of accepted members does not change. For the purpose of fitting chemical evolution models, we additionally excluded stars that have either [Fe/H] random uncertainties or [α/Fe] random uncertainties that exceed 0.3.

There are 56 objects that are And XVIII members. The 57th object is the most metal-rich star in our sample. We argue below that it is a member of M31's halo, not that of And XVIII. The membership list for the derivation of the chemical evolution models' parameters contains 38 stars after excluding the most metal-rich star.

4.1.1. Contamination from M31 Halo Stars

It is impossible to completely remove foreground and background objects with 100% confidence. In particular, since PAndAS9654 has a higher metallicity than the other 38 members, we discuss our reasons for counting it as a member of the M31 halo, rather than that of And XVIII.

This star is shown in Figure 6 as the most metal-rich star, with [Fe/H] = −0.575, [α/Fe] = 0.503, and in Figure 3 as a yellow star symbol. Figure 2 shows how PAndAS9654 is distinct from members of And XVIII. Metal-rich stars are expected to be on the red side of the red giant branch (RGB), but PAndAS9654 appears on the blue (left) side of And XVIII's RGB. This position would be expected if it is a less luminous star but at a lower distance modulus than And XVIII.

Therefore, in order to further consider its membership in And XVIII, we tried the velocity method used by Collins et al.

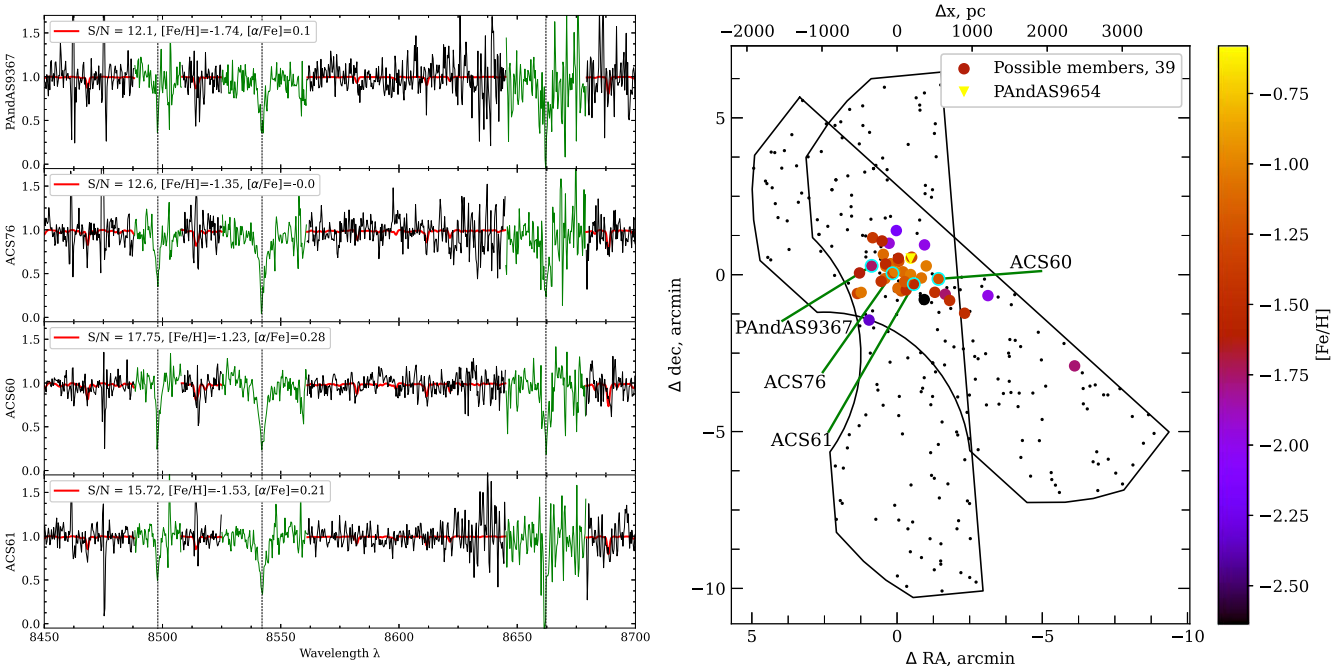

Figure 3. Left: Examples of member stars spectra with different S/N. Figure 3 (right) contains their subscripts. Black is used to indicate normalized flux; green indicates spectral regions excluded from abundance analysis; red is for interpolated synthetic spectra with [Fe/H] and [α/Fe] as indicated in the plot's legend; and vertical lines mark the Ca triplet lines. Right: Map of And XVIII stars color-coded by metallicity. Small black points are nonmembers. The two DEIMOS slitmasks are shown with outlines.

(2013). The authors developed the method to consider the probability that each star belongs to one of three velocity Gaussians: the MW, M31's halo, and the dwarf galaxy. This approach is reasonable, but it is limited by the strong overlap between the Gaussians for M31's halo and And XVIII. Figure 4 shows how PAndAS9654 overlaps with And XVIII radial velocity and spatial distribution, while Figure 5 shows the velocity distribution of 170 observed objects along with Gaussians that represent the mean and standard deviation of velocities in M31, the MW, and And XVIII (the rest of the observed objects have radial velocities outside of the plot's range: $v_{\rm helio} < -400\,{\rm km\,s^{-1}}$ or $v_{\rm helio} > 100\,{\rm km\,s^{-1}}$). All M31 and MW halo parameters that we used were taken from Collins et al. (2013). The normalization of the Gaussians in the figure is arbitrary. The metal-rich star already passed the velocity membership test. To sum up, the velocity criterion does not solve all of the difficulties in determining secure dwarf galaxy's stars.

For this reason, Tollerud et al. (2012) used the set of membership criteria that does not include velocity, and they also emphasized that it is difficult to distinguish M31 halo stars from satellite members. The authors mentioned the importance of metallicity differences between satellite populations of M31 ([Fe/H] ≈ -1.4 to -2.0) and M31 halo stars ([Fe/H] ≈ -1.5 to -0.1), although they used photometrically derived metallicities. A more thorough way to consider membership in the M31 halo was studied by Gilbert et al. (2012) and references therein. Based on their success rate of recovering M31 members as a function of distance from M31's center, a DEIMOS observer may expect about 1–3 M31 halo stars per slitmask at a projected radius of $\approx$114 kpc, which corresponds to And XVIII (see Appendix C). And XVIII's three-dimensional distance is 579 kpc *behind* M31. Therefore, we must look through the entirety of M31's halo to see And XVIII, thus increasing the possibility of contamination by halo stars.

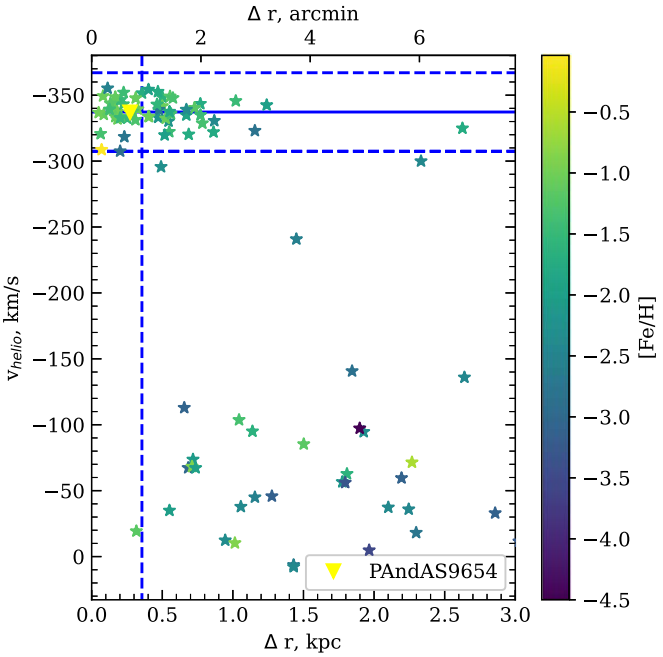

Figure 4. Radial velocity vs. projected distance from the center of And XVIII. Horizontal lines correspond to $\langle v_{\rm helio}\rangle$ of the dwarf galaxy and a $3\sigma_v$ region around it. The vertical line corresponds to the half-light radius ($r_{1/2}$) calculated with the McConnachie et al. (2008) angular value and Makarova et al. (2017) distance (see Table 4). The reader may compare the plot with Figure 12 of Tollerud et al. (2012) from the SPLASH overview of M31 satellite system.

These arguments support our assessment that PAndAS9654 is more likely a member of M31 than of And XVIII. It was the only star that we additionally excluded as an M31 halo member, because its CMD position is inconsistent with its spectroscopic metallicity, and its metallicity is much higher than any other member star (Figures 2, 3, and 6). For that

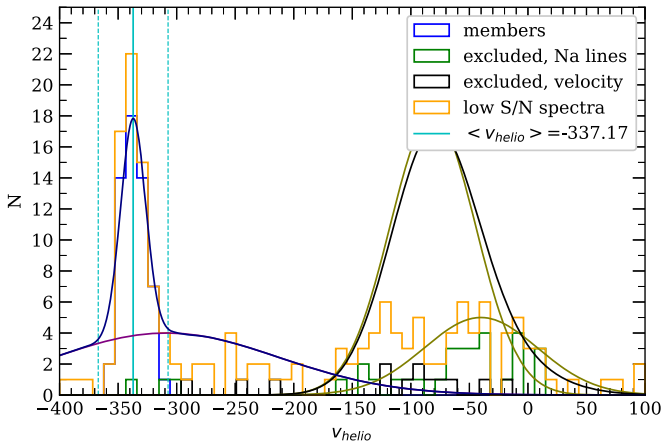

Figure 5. Velocity distribution. The objects that were excluded due to the presence of strong Na I 8195 lines are shown in green. The objects that were excluded due only to the velocity criterion are shown in black. The yellow histogram includes the 170 objects from both and18a and and18b slitmasks within the radial velocity range shown. Also shown are the approximate shapes of velocity distributions for MW stars (combination of the disk and halo with $\langle v_{\rm mw1}\rangle = -81.2$ km s^{-1}, $\sigma_{\rm mw1} = 36.5$ km s^{-1}, $\langle v_{\rm mw2}\rangle = -40.2$ km s^{-1}, $\sigma_{\rm mw2} = 48.5$ km s^{-1}) and the Andromeda halo ($\langle v_{\rm M31}\rangle = -308.8$ km s^{-1}, $\sigma_{\rm M31} = 96.3$ km s^{-1}; Collins et al. 2013) on the plot. The approximate fraction of M31, MW, and And XVIII stars among 170 objects for Gaussians were derived using Collins et al. (2013) approach. The normalization of the velocity distribution is arbitrary.

reason, we estimated kinematical properties for both data sets —with and without PAndAS9654—to compare its impact on the results.

At the same time, we are not excluding any other metal-rich stars from their CMD position. Specifically, Boyer et al. (2015) and Goldman et al. (2019) obtained infrared photometry of some Local Group dwarf galaxies, including And XVIII. They statistically derived upper limits for the numbers of TRGB and approximate giant branch (AGB) stars. Boyer et al. found that And XVIII appears to have one of the largest populations of AGB stars, although Goldman et al. later found no pulsating AGB stars. There are two main implications of their surveys that are relevant for this work. First, the two stars from HST photometry brighter than the TRGB may indeed belong to the AGB population of And XVIII and therefore may still be members (see Figure 2). Second, this dwarf galaxy must have faced star formation at some recent time, because bright AGB stars are at least intermediate in mass. Their presence lends support to the younger ages found in the SFH (Makarova et al. 2017).

4.2. Kinematics

We measured the galaxy's kinematics by first assuming that $v_{\rm rot} = 0$ (Equation (7)). We used MCMC to find the most likely values of $\langle v_{\rm helio}\rangle$ and σ_v. After <10 MCMC trial runs for membership determination, with 5 walkers consisting of 1000 iterations each, we labeled 57 stars as probable velocity members of And XVIII (see Section 4.1).

We evaluated the kinematic properties both including and excluding PAndAS9654, although the difference in the derived $\langle v_{\rm helio}\rangle$ is 0.1 km s^{-1}: -337.3 km s^{-1} with PAndAS9654 and -337.2 km s^{-1} without. Then, we calculated the two parameters in 10^5 iterations. For the rest of this paper, we quote values derived with the exclusion of PAndAS9654 (56 members).

Next, we tried to derive whether And XVIII rotates by maximizing the likelihood in Equation (8) with MCMC. In this case, 10^6 iterations converged to nearly the same $\langle v_{\rm helio}\rangle$ and σ_v as the previous trial. The derived rotation velocity is significantly lower than the velocity dispersion (see Table 2). This means that And XVIII is a dispersion-supported dwarf galaxy (it does not exhibit significant rotation).

We estimated the dynamical mass within the half-light radius, $\log(M_{1/2}/M_\odot)$, using $M_{1/2} = 3\sigma^2_{\rm los} r_{1/2} G^{-1}$ from Wolf et al. (2010) and the half-light radius from McConnachie et al. (2008) (see Table 4). The use of this equation is justified because And XVIII is a dispersion-supported galaxy.

4.3. Metallicity

We measured a mean metallicity of $\langle$[Fe/H]$\rangle = -1.49$ and a dispersion of $\sigma_{\rm [Fe/H]}$=0.36 by fitting a Gaussian to the metallicity distribution. The luminosity–metallicity relation (Kirby et al. 2013) predicts that the mean metallicity of And XVIII would be [Fe/H] $= -1.65 \pm 0.16$, using the luminosity computed by Makarova et al. (2017). This prediction is consistent at 1σ with our measurement of $\langle$[Fe/H]$\rangle = -1.49$.

Although we measured reliable abundances (less than 0.3 dex random uncertainties) for only 38 member stars (and PAndAS9654), they show a clear metallicity gradient (Figures 3 and 6). Using the least-squares method, for 37 And XVIII members excluding PAndAS8654 and the most distant star, we measured

$$\nabla_{\rm [Fe/H]}(r/r_{1/2}) = -0.23 \pm 0.03 \text{ dex } r_{1/2}^{-1} \quad (9)$$

for the linear metallicity profile approximation. We also recalculated the gradient, excluding the next two outermost stars to examine whether they heavily influence the measured gradient:

$$\nabla_{\rm [Fe/H]}(r/r_{1/2}) = -0.29 \pm 0.04 \text{ dex } r_{1/2}^{-1}. \quad (10)$$

The uncertainties on these intervals are calculated from the Python function `scipy.optimize.curve_fit` (Virtanen et al. 2020). The errors on the gradient do not include the negligibly small uncertainties on the distance from the center, r.

Leaman et al. (2013) and Taibi et al. (2022), in their dwarf galaxy surveys, emphasized the importance of angular momenta, stellar mass, internal feedback (SFH), and galaxy interactions for the formation of metallicity gradients. The relationship and influence of these parameters remain obscure. The main Taibi et al. result is that the biggest metallicity gradient could be caused by dwarf–dwarf mergers. Possible galaxies for which this happened include And II, Phoenix, Sextans, Fornax, and NGC 6822 (Taibi et al. 2022, and references therein). The steep spatial metallicity gradient of And XVIII seems to be in accordance with this set of dwarfs. Leaman et al. found that dIrrs often have shallow metallicity gradients, whereas dSphs have larger gradients. And XVIII conforms to this distinction. However, in a larger set of dwarf galaxies, Taibi et al. could not corroborate the relation between dwarf galaxy morphology and strength of metallicity gradient. We discuss some further And XVIII's metallicity properties in the next sections and in Figures 7 and 8.

4.4. Detailed Abundance Ratios

The Tinsley ([α/Fe]–[Fe/H]) diagram provides details about the SFH of And XVIII (Figure 8). The [α/H] of the galaxy increases due to core-collapse (Type II) supernovae, while

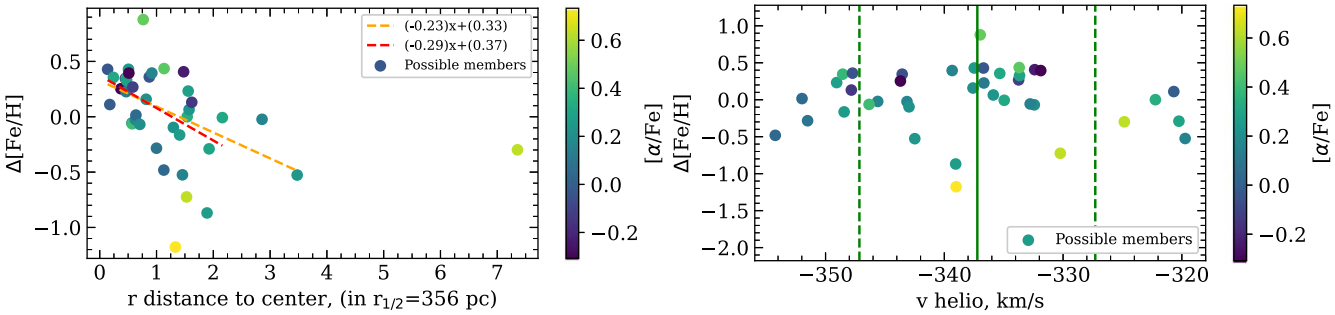

Figure 6. Left: Metallicity distribution with the distance to the center color-coded by [α/Fe]. The point with the largest [Fe/H] is the star PAndAS9654 (see Section 4.1). Right: Metallicity vs. $v_{\rm helio}$ color-coded by [α/Fe]. Here, $v_{\rm helio}$ and σ_v are shown with solid and dashed lines, respectively.

Table 4
Properties of Andromeda XVIII

Research	α, δ	m–M	$R_{\rm helio}$, kpc	$R_{\rm M31}$, kpc	$r_{1/2}$, arcmin	$\log(r_{1/2}/{\rm kpc})$
McConnachie et al. (2008)	00 02 14.5^{+10}_{-10} 45 05 20^{+10}_{-10}	$25.66^{+0.13}_{-0.13}$	1355^{+88}_{-88}	589	$0.92^{+0.05}_{-0.06}$	$-0.44^{+0.036}_{-0.041}$
Tollerud et al. (2012)	–[a]	…	$1355^{+83.6,\ a}_{-78.8}$	$590.9^{+87.5,\ a}_{-82.6}$	…	$-0.38^{+0.03,\ a}_{-0.03}$
Conn et al. (2012)	–[a]	$25.42^{+0.07}_{-0.08}$	1214^{+40}_{-43}	457^{+39}_{-47}	…	…
Collins et al. (2013), Section 4	–[a]	…	$1214^{+40,a}_{-43}$	…	…	$-0.49^{+0.031,a}_{-0.033}$
Makarova et al. (2017)	–[a]	$25.62^{+0.09}_{-0.17}$	1330^{+60}_{-90}	$579.^{+87.}_{-87.}$	…	…
Wojno et al. (2020)	–[a]	…	…	…	…	
This work	–[a]	$25.62^{+0.09,\ a}_{-0.17}$	$1330^{+60,\ a}_{-90}$	$579^{+87.,\ a}_{-87.}$	$0.92^{+0.05,\ a}_{-0.06}$	$-0.45^{+0.032}_{-0.07}$

[Fe/H] (oldest)	[Fe/H] (inter)	$N_{\rm mem}$	$v_{\rm helio}$	σ_v	$\log(M_{1/2}/M_\odot)$	E_{B-V} used	M_V	$\log(L_{1/2}/L_\odot)$
$-1.8^{+0.1}_{-0.1}$		…	…	…	…	0.104	< -9.7	…
–		22	$-332.1^{+2.7}_{-2.7}$	$9.7^{+2.3}_{-2.3}$	$7.43^{+0.24}_{-0.24}$	…	$-9.7^{+0.1,\ a}_{-0.1}$	$5.49^{+0.03,\ a}_{-0.03}$
–		…	…	…	…	0.104	…	…
$-1.4^{+0.3}_{-0.3}$		4	$-346.8^{+2.0}_{-2.0}$	$0.0^{+2.7}$	$0^{+6.15}$	…	-9.7^{a}	…
$-1.74^{+0.20}_{-0.20}$	$-1.33^{+0.20}_{-0.20}$	…	$-332.1^{+2.7,\ a}_{-2.7}$	$9.7^{+2.3,\ a}_{-2.3}$	$6.62^{+0.03,\ b}_{-0.03}$	0.093	$-10.41^{+0.28}_{-0.28}$	…
$-1.33^{+0.02}_{-0.02}$		20	$-332.1^{+2.7,\ a}_{-2.7}$	…	$5.9^{+0.3,\ b}_{-0.3}$	…	…	…
$-1.49^{+0.36}_{-0.36}$		38	$-337.2^{+1.5}_{-1.4}$	$10.0^{+1.1}_{-1.0}$	$7.38^{+0.12}_{-0.17}$	…	…	…

Notes.
[a] Values adopted from other works.
[b] Total measured stellar mass.

[Fe/H] increases due to both Type II SNe and thermonuclear (Type Ia) supernovae. The Type Ia SNe explode only after a time delay of one Gyr—hundreds of Myr. A shallower slope of the [α/Fe]–[Fe/H] relation indicates that both types of SNe were exploding at similar rates, which means relatively continuous star formation. The [α/Fe] knee indicates when Type Ia SNe dominated over Type II SNe. A steep decline in [α/Fe] reflects a period of waning star formation, when Type II SNe were less frequent but Type Ia SNe were continuing to explode. The slope of [α/Fe] for [Fe/H] > -1.5 indicates that the star formation rate was steeply declining during this period of the galaxy's life.

4.5. Chemical Evolution Models

In Section 3.4, we described analytic chemical evolution models of galaxy metallicity distributions under the assumption of instantaneous recycling. While this is a good assumption for α elements, [Fe/H] is created copiously by Type Ia SNe, and thus iron is a delayed element that violates the instantaneous recycling approximation. On the other hand, the errors for [α/H], which are derived as

$$\delta[\alpha/{\rm H}]_i = \sqrt{\delta[\alpha/{\rm Fe}]_i^2 + \delta[{\rm Fe/H}]_i^2 + 0.106^2} \quad (11)$$

(where 0.106 is the systematic error on [α/H], per Kirby et al. 2010), are bigger than the [Fe/H] errors, so fits to the [Fe/H] distribution are more reliable. To compare the models, we used the AICc:

$$\mathrm{AICc} = -2\ln L + 2r + \frac{2r(r+1)}{N-r-1}, \quad (12)$$

where L is the likelihood, r is the number of model parameters, and N is the number of stars. The smaller the AICc, the better the model.

The parameters derived from the [Fe/H] distribution (Figure 7, right) for the Leaky Box and Pre-Enriched models are qualitatively similar for these models. The Accretion model well describes the overall shape of the distribution, giving And XVIII's current mass in units of its initial mass as $M \approx 3.4$. The Accretion model is the most appropriate of these three models, according to its AICc, so we conclude that And XVIII experienced gas infall during its star formation lifetime. That infalling gas could be the return of gas after tidal stirring, a wet merger with another dwarf galaxy, or accretion of gas from the intergalactic medium (IGM).

All three of these models fail to account for the sharp metal-rich cutoff at [Fe/H] ≈ -1. The Ram Pressure Stripping (RPS)

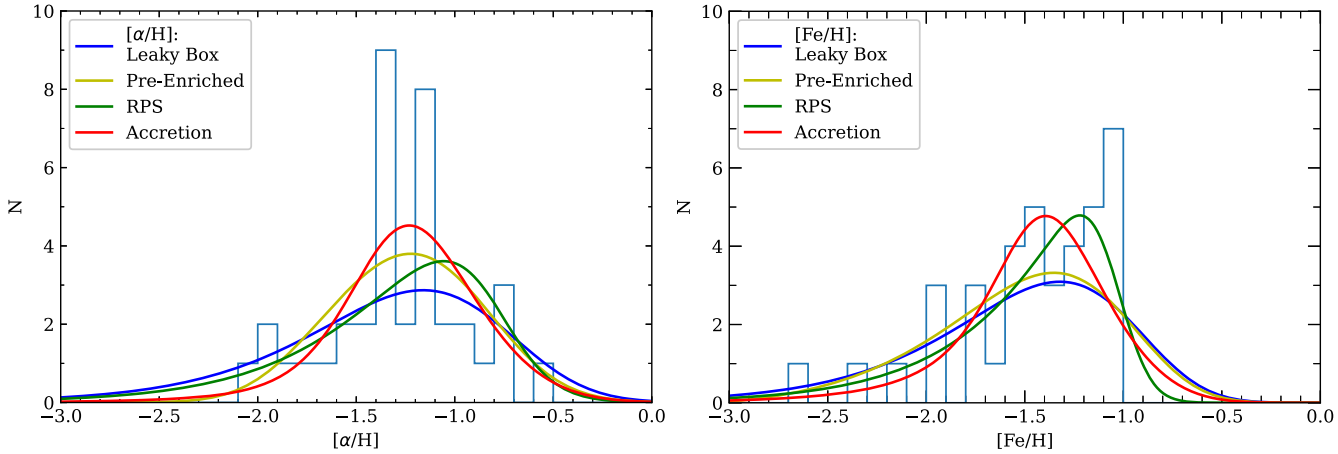

Figure 7. Metallicity distributions for [α/H] (left) and [Fe/H] (right) in And XVIII. The metal-rich end of the [Fe/H] distribution appears to be sharply truncated, but that truncation is less apparent in [α/H]. The best-fit chemical evolution models, convolved with the error kernel of the measurements, are shown as colored curves.

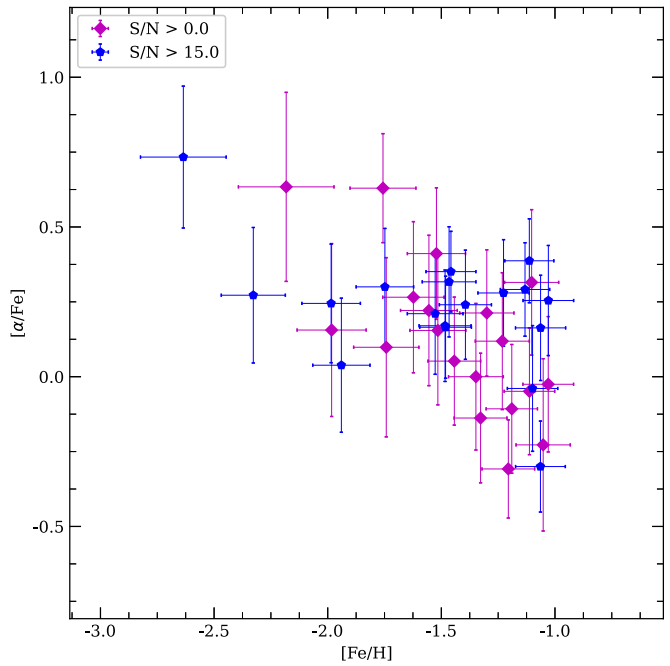

Figure 8. Tinsley diagram ([α/Fe] vs. [Fe/H]) for 38 stars, excluding PAndAS9654. Stars with S/N $>$ 15 are shown in blue; those with lower S/N are shown in purple.

model seems to solve this problem. Comparison of the best-fit stripping intensity ($\zeta \approx 4.6$) with some other dwarf galaxies (Kirby et al. 2013) indicates that And XVIII is among the most ram-pressure-stripped galaxies known. Furthermore, the best model is RPS, according to its AICc (Table 3).

The [α/H] histogram for And XVIII exhibits a rather different picture (Figure 7, left). Both the Pre-Enriched and Accretion models seem to describe the [α/H] distribution better than the RPS one. The RPS model is not required to explain the [α/H] distribution, due to the presence of a metal-rich tail. As noted by Leaman et al. (2013), the preference of the Pre-Enriched model can be caused by the undersampling of the metal-poor tail of the stars, although the [Fe/H] distribution contains a metal-poor tail. Our conclusions might be affected here by the spatial selection function of And XVIII's members, coupled with its metallicity gradient (Figure 6), which is more important than the sample size bias, as also shown by Leaman et al. (2013).

Thus, we have arrived at different conclusions depending on whether we treated metallicity as Fe or α. However, the smaller errors on [Fe/H] make the [Fe/H] results more significant, so we cannot rule out the possibility that And XVIII faced ram pressure stripping in its past.

5. Discussion

In this section, we consider the evidence in support of or against three hypotheses for the origin of the dSph nature of And XVIII: the backsplash hypothesis, the merger hypothesis, and the self-quenching hypothesis. This evidence comes from the above results, as well as some previous references, some of which are listed in Table 4. For example, for the backsplash hypothesis, we consider whether the existing observations of the kinematics and chemical evolution of And XVIII support the hypothesis that it once passed through the virial radius of M31 (which is more than 200 kpc; Gilbert et al. 2012; Tollerud et al. 2012).

To emphasize the principal difference of the last hypothesis, it is important to mention that we do not have direct evidence whether the cause of this gas loss was an internal process, like feedback, or an external process, like stripping by M31. Internal processes, like gas stabilization after prolonged star formation or internal feedback (i.e., from supernova explosions and winds from low-mass stars) are not expected to be the main drivers of gas removal in dwarf galaxies (Weisz et al. 2011, and references therein). Weisz et al. found that SFHs in dIrrs and dSphs are distinct in the recent past, especially within 1–2 Gyr. And XVIII's comparatively continuous star formation for several Gyr prior to ceasing 1.5 Gyr ago (Makarova et al. 2017) might indicate that external processes, such as ram pressure stripping or tidal stirring, completely removed all of And XVIII's star-forming gas in the recent past. However, internal processes are known from simulations and observations of the oldest stellar populations to be most important early in the Universe. DSphs, most of which formed the majority of their stars more than 10 Gyr ago, seem to lose their gas due to intensive Type II supernova feedback (e.g., Bermejo-Climent et al. 2018). Deeper photometry of And XVIII that reaches the main-sequence turn-off of old populations can also improve the precision of the SFH at old times. From those future observations, we can better infer the role of internal processes on gas loss at early times.

We also emphasize the importance of membership determination in our conclusions. Membership in And XVIII is especially complicated due to the galaxy's distance and possible confusion with M31 halo stars. All of our conclusions are predicated on the assumption that our sample contains very few nonmembers.

5.1. Backsplash Hypothesis

5.1.1. Stellar Population

If And XVIII is a backsplash galaxy, it could have experienced ram pressure stripping during its pericentric flyby. In this context, it is useful to know the amount of remaining gas. Spekkens et al. (2014) estimated an H I mass upper limit of $4.8 \times 10^6\,M_\odot$ for a distance of 1.21 Mpc (McConnachie 2012). Corrected to 1.33 Mpc, the limit would be $5.8 \times 10^6\,M_\odot$. The nondetection of H I is consistent with ram pressure stripping, but the upper limit is too large to be definitive (Appendix B).

However, the SFHs determined by Makarova et al. (2017) and Weisz et al. (2019) using different CMD models might support ram pressure stripping in the past. They used HST photometry, although it was not deep enough to reach the main-sequence turn-off of the oldest stars. For that reason, both works mentioned the low precision for the 12–14 Gyr period. Makarova et al. (2017) discussed in detail the presence of old and intermediate populations in And XVIII based on the oblong red clump shape. The periods of star formation are 12–14 Gyr ago and about 1.5–8 Gyr ago, with a starburst 8 Gyr ago and full quenching at 1.5 Gyr ago. The authors explained such a recent truncation as natural gas loss (due to supernova winds, for example) without the need for an external mechanism of gas loss. Despite that, the metallicity distribution of And XVIII has a sharp metal-rich truncation (Figure 7). As a result, the metal-poor tail appears consistent with a Leaky Box or Accretion model, which suggests that And XVIII was forming stars like a normal isolated dwarf galaxy, but then the sharp drop at $[\mathrm{Fe/H}] \sim -1$ is consistent with neither of these models.

The $[\alpha/\mathrm{Fe}]$–$[\mathrm{Fe/H}]$ diagram also supports a complex SFH. The shallow slope of $[\alpha/\mathrm{Fe}]$ at $[\mathrm{Fe/H}] \lesssim -1.5$ is consistent with the analogous diagram for And XVIII obtained from coadded spectra by Wojno et al. (2020), although they have a smaller sample. As already mentioned (Section 3.3), this shape of the curve indicates the relative frequency of Types II and Ia SNe. When the galaxy had a metallicity $[\mathrm{Fe/H}] \lesssim -1.5$, the rates of the two types of SNe were comparable. This confirms that the galaxy had a sufficient gas mass to power star formation for a while. After that, at $[\mathrm{Fe/H}] \gtrsim -1.5$, the slope of $[\alpha/\mathrm{Fe}]$ decreases steeply. Thus, we conclude that the gas loss began in earnest when the metallicity was in the range $-1.5 < [\mathrm{Fe/H}] < -1.0$.

5.1.2. Kinematics

Now we consider And XVIII's orbit around M31, testing whether it is kinematically consistent with being a backsplash galaxy. We use Teyssier et al. (2012) definition of a backsplash galaxy: objects on extreme orbits that have taken them through the inner $0.5\,R_{\rm vir}$ of a larger potential and subsequently carried them back outside $R_{\rm vir}$. From cosmological Via Lactea II simulations, Teyssier et al. estimated the fraction of this type of galaxy at about 13% for the Local Group. Tollerud et al. (2012) measured a radial velocity and a velocity dispersion of And XVIII from the SPLASH overview of M31 satellite system. They found that And XVIII is bound to M31 and possibly near its apocenter. Therefore, it might have once passed close to M31, qualifying it as a backsplash galaxy.

Starting from the two-body problem (And XVIII and M31), we can consider five observables: the distances between And XVIII, M31, and the MW, and the heliocentric radial velocities of And XVIII and M31. The three-dimensional distance between And XVIII and M31 is 579 kpc (Makarova et al. 2017), and their relative velocity is $-36\,\mathrm{km\,s^{-1}}$ using an M31 heliocentric velocity of $-301\,\mathrm{km\,s^{-1}}$ from Karachentsev & Kashibadze (2006) (approximating the angle between the M31 line of sight and the And XVIII line of sight as zero). And XVIII's total orbital energy is negative if we assume that it has no tangential velocity component. For these assumptions, the highest tangential velocity to keep the system bound is about $154.5\,\mathrm{km\,s^{-1}}$ relative to M31. For such a value, the proper motion relative to M31's proper motion will be about $24.5\,\mu as\,\mathrm{yr^{-1}}$. There are no current measurements of its proper motion.

Next, using the virial theorem and the energy conservation law, along with the observed kinetic energy per unit mass estimated from its radial velocity only, we obtain a semimajor axis of about 305 kpc. Then, with Kepler's laws and M31's mass of $\approx 1.69 \times 10^{12}\,M_\odot$ (van der Marel et al. 2012b), its orbital period is about 12 Gyr. The time since its closest passage through M31 is about 7.8 Gyr (see Appendix C). Around the same lookback time, And XVIII experienced a spike in SFR (Makarova et al. 2017). Di Cintio et al. (2021) discussed how a pericentric passage could actually increase SFR, and Miyoshi & Chiba (2020) found that observed dwarf galaxies reached their peak SFR at the time of infall (presumably right before their gas was stripped). Nonetheless, And XVIII's minimum pericentric distance could be as small as 1.2 kpc, which is well within the range required for ram pressure stripping and significant tides. Appendix B gives further details about the RPS dependence on the unknown tangential velocity, and in Appendix C we consider the two-body modeling results for the backsplash hypothesis in greater detail than the rough discussion here.

We can also consider the three-body (And XVIII, M31, and the MW) problem without accounting for interaction between the MW and M31, i.e., assuming binary-like motion of the large galaxies. The current distance between M31 and And XVIII (579 kpc) is comparable with the distance of M31 to the MW (about 770 kpc; van der Marel et al. 2012b; Karachentsev & Kashibadze 2006). Taking into account the ratio of M31's mass to the MW—about two to three—the Roche lobe of M31 is expected to be more extended than the MW's, with a radius about 2/3 of the distance between the two galaxies. Knebe et al. (2011) investigated renegade dwarf galaxies, which change their host galaxy. However, the dynamical modeling in Appendix D excludes the possibility of And XVIII orbiting the MW in the past. Our three-body model indicates that And XVIII could have experienced a flyby of M31 at about 7–10 Gyr ago, depending on the unknown tangential velocity of And XVIII relative to M31's tangential velocity (see Appendix D).

For simplicity, we did not consider cosmological effects. With a Hubble constant of $H_0 = 68\,\mathrm{km\,s^{-1}\,Mpc^{-1}}$ (see DESI Collaboration et al. 2024), the current cosmological recession velocity of And XVIII is $90\,\mathrm{km\,s^{-1}}$ relative to the MW and

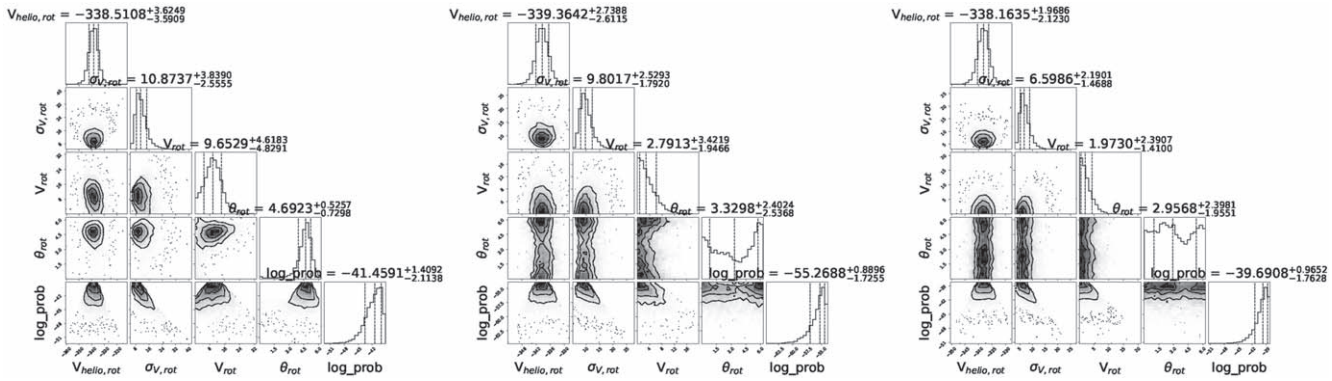

Figure 9. From left to right: MCMC corner plots for rotational models of secure And XVIII members in the metallicity bins [Fe/H] < -1.6, $-1.6 <$ [Fe/H] < -1.25, and [Fe/H] > -1.25. The parameters are mean heliocentric velocity ($v_{\rm helio,rot}$), velocity dispersion ($\sigma_{v,\rm rot}$), rotation velocity ($v_{\rm rot}$), and position angle ($\theta_{\rm rot}$). The likelihood is "prob."

39 km s^{-1} relative to M31. Therefore, there is a future opportunity to explore more sophisticated dynamical models.

In addition, the passage through a large host leads to tidal stirring or ram pressure stripping (Teyssier et al. 2012). From Figure 1 and Higgs & McConnachie (2021), we can see that And XVIII has an oblong shape, which could be a sign of past tidal stripping (see Bennet et al. 2018). However, an increase in SFR, such as that inferred by Makarova et al. (2017), is not necessarily expected in these interactions. On the other hand, interaction with a smaller (comparably sized) companion could increase the SFR (D'Onghia et al. 2009; Lelli et al. 2014). The next section considers this possibility.

The most consequential assumption here is the neglect of the tangential component of And XVIII's orbital velocity. And XVIII appears behind M31 on its assumed orbit around M31, so the tangential component of its velocity could be larger than the radial component, unless the orbital ellipticity is close to one. Some dwarf galaxies are on highly radial orbits (Simon 2018; Li et al. 2021), so it is certainly possible that And XVIII is on such an orbit. Nonetheless, we cannot definitely say that And XVIII is bound to M31 in the absence of tangential velocity. Future observations with HST, JWST, Roman, or Euclid might be able to measure proper motion with the precision to rule out a bound orbit (e.g., Libralato et al. 2023).

5.2. Merger Hypothesis

For the merger hypothesis, we can consider some inferences from And XVIII's internal kinematics. The signs of a major merger may include prolate rotation, starbursts, resonant ram pressure stripping, differences in the young and old stellar populations, and a steep metallicity gradient (D'Onghia et al. 2009; Lelli et al. 2014; Cardona-Barrero et al. 2021). Some of these properties are present in And XVIII. The galaxy did experience an increase in SFR 7.5 Gyr ago, followed by a period of continuous star formation (Makarova et al. 2017). That continuation of star formation does not support the idea of a backsplash galaxy, wherein the interaction with a large galaxy is expected to remove all gas from the dwarf galaxy. However, it could be consistent with a major merger. Furthermore, And XVIII does have a steep metallicity gradient (Figure 6), which is also true for the suspected merger remnants with prolate rotation (And II and Phoenix; Cardona-Barrero et al. 2021).

We investigated kinematic differences between the older and younger populations, identified by Makarova et al. (2017) as being split at [Fe/H] $= -1.6$ and -1.25. Each group ([Fe/H] < -1.6, $-1.6 <$ [Fe/H] < -1.25, [Fe/H] > -1.25) contains 10–15 stars. Figure 9 presents the most likely parameters for the model with rotation (Equation (8)). Although all three groups are dispersion-supported, the dispersion for the two more metal-rich (younger) groups is lower, and the oldest stars are the most dynamically heated. Evidence for rotation—though not very significant—is the strongest in the most metal-poor bin. The rotation axis position angle for the most metal-poor group is close to the semimajor axis defined by Higgs & McConnachie (2021), who measured the galaxy's ellipticity to be about 0.4 and the position angle to be 75°.12 (4.45 rad, while 4.69 rad was obtained for the positional angle of the rotational axis for the most metal-poor stars); see Figure 9. Thus, there is a possibility that And XVIII's older stars exhibit prolate rotation.

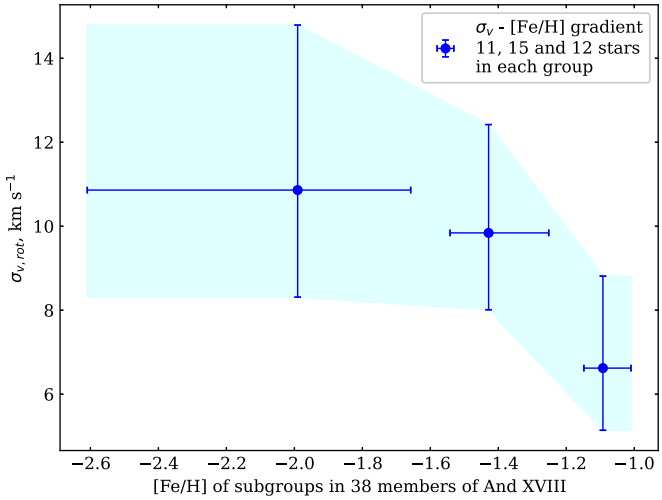

Figure 10. Velocity dispersion estimated for secure And XVIII members in metallicity bins [Fe/H] < -1.6, $-1.6 <$ [Fe/H] < -1.25, and [Fe/H] > -1.25, calculated with the rotational kinematical model. This result is in correspondence with the observed kinematic gradient in Figure 6 (right).

The merger of two gas-rich dwarf galaxies is theorized to induce centrally concentrated star formation with a velocity dispersion and radial extent smaller than the pre-merger population (Benítez-Llambay et al. 2016). The merger drives gas to the center, where it is completely expended in new star formation and feedback-driven ejection (Taibi et al. 2022). Figure 3 (right) and Figure 10 show that the metal-poor stars have a larger velocity dispersion than the metal-rich stars. The

latter plot was obtained after the application of the rotational kinematic model for metallicity subgroups in And XVIII. The comparatively dynamically hot metal-poor fraction of And XVIII stars may support the hypothesis that it originated in the merger of two roughly equal-sized dwarf galaxies (Walker & Peñarrubia 2011; Genina et al. 2019).

5.3. Self-quenching Hypothesis

The measured SFH of And XVIII (Makarova et al. 2017) suggests extended star formation, even after the time of its possible close passage by M31. It would be unusual for a dwarf galaxy of And XVIII's stellar mass to survive ram pressure stripping. Therefore, it is possible that it was not ram pressure stripped or even a product of a major merger. Instead, it could have quenched itself.

Arimoto & Yoshii (1987) presented a galactic chemical evolution model wherein supernovae drive a wind from the galaxy. For galaxies with a gas mass $\lesssim 4 \times 10^9\,M_\odot$, the wind becomes a "terminal wind," which removes all gas from the galaxy and quenches it. The resulting metallicity distributions can be sharply truncated at the metal-rich end, essentially because the wind interrupts the galaxy's otherwise closed-box chemical evolution.

Observed metallicity distributions of dwarf galaxies (e.g., Kirby et al. 2011) rarely show such a sharp truncation. This is especially true for isolated dwarf irregular galaxies (Kirby et al. 2013). Therefore, And XVIII would be unique among known isolated galaxies if it were self-quenched by a terminal wind.

Makarova et al. (2017) SFH was observed from shallow HST images—just one orbit per filter. Therefore, the SFH was measured almost entirely from the red clump. A much more precise SFH could be determined from photometry that reaches the old main-sequence turn-off. Those observations would require much deeper space-based photometry, such as by many more orbits with HST or with a moderate investment of time on JWST.

6. Conclusion

We derived the kinematic and chemical properties of And XVIII. And XVIII is a dispersion-supported spheroidal galaxy. Sharp truncation in the [Fe/H] distribution might indicate sudden gas stripping, such as ram pressure during a close passage by M31. The [α/Fe]–[Fe/H] diagram is consistent with the extended (but now quenched) SFH found by Makarova et al. (2017). We considered three possible theories of And XVIII's origin:

1. And XVIII is a backsplash galaxy that once passed close to M31. With a small enough (yet unknown) tangential velocity, its radial velocity relative to M31 indicates that it is bound to M31. The position on the luminosity–metallicity diagram suggests past tidal interaction, which would have led to gas loss and would have truncated the SFH.
2. And XVIII is the result of the merger of two comparably sized dwarf galaxies. Its velocity dispersion gradient and metallicity gradient are well explained by this type of interaction.
3. Because isolated dwarf galaxies are rarely quenched, it is plausible that past environmental interaction rather than internal feedback quenched And XVIII (e.g., Weisz et al. 2011). Nonetheless, we cannot rule out that And XVIII quenched itself without stronger evidence of past environmental interactions.

The observed orbital energy of And XVIII is consistent with the backsplash hypothesis. Alternatively, the SFH and metallicity gradient are consistent with the merger hypothesis. The inconsistency of both suggestions could mean that internal processes account for the expected gas loss, after all. Measuring a proper motion could disprove the backsplash hypothesis by proving that And XVIII is not bound to M31.

We conclude that the balance of the evidence slightly favors a backsplash origin to And XVIII, which is weakly associated (using the terminology of Teyssier et al. 2012) with M31. Its passage through M31 could have happened about 10 Gyr ago. Instead of quenching all star formation as it passed through the host galaxy, it first intensified star formation and later lost its gas.

Overall, some of the evidence we have presented supports each of the above three hypotheses, and some of it is mildly inconsistent with each of them. Additional data—especially deeper, second-epoch space-based imaging taken about a decade after the first-epoch HST imaging—will help resolve how And XVIII became an unusually quiescent yet isolated dwarf galaxy.

Acknowledgments

We thank L. Makarova for sharing the HST photometry catalog. E.N.K. acknowledges support from NSF CAREER grant AST-2233781. R.L.B. acknowledges support from NSF grants AST-0307842, AST-0607726, AST-1009882, and AST-1413269 for the SPLASH photometry and AST-2108616. Based in part on observations at NSF Kitt Peak National Observatory, NSF NOIRLab (NOIRLab Prop. ID 2010B-0596; PI: R. Beaton), which is managed by the Association of Universities for Research in Astronomy (AURA) under a cooperative agreement with the U.S. National Science Foundation. The authors are honored to be permitted to conduct astronomical research on I'oligam Du'ag (Kitt Peak), a mountain with particular significance to the Tohono O'odham.

Facility: Keck:II (DEIMOS) Mayall (MOSAIC-1 wide-field camera).

Software: astropy (Astropy Collaboration et al. 2013, 2018, 2022), corner (Foreman-Mackey 2016), emcee (Foreman-Mackey et al. 2013), matplotlib (Hunter 2007), numpy (van der Walt et al. 2011), scipy (Virtanen et al. 2020), DAOPHOT (Stetson 1987), DAOGROW (Stetson 1990), ALLFRAME (Stetson 1994).

Appendix

In these appendices, we further investigate the possibility of a close passage of And XVIII by M31 and that flyby's hypothetical ability to truncate star formation. The following sections consider the RPS criterion (Gunn et al. 1972), possible orbits of And XVIII around M31 within a two-body interaction, and some possible orbits of And XVIII within a three-body problem. To simplify the orbital modeling, we will consider only those orbits that lie within the plane, which is derived from the current positions of MW, M31, and And XVIII. To make all terms as clear as possible, we also describe here the applied coordinate transformation.

Appendix A
Coordinate Transformation

M31's velocity within the equatorial system was taken as (125.2, −73.8, −301.) km s^{-1}; the distance of 770 kpc and the proper motion along R.A. and decl. directions are from van der Marel et al. (2012b); and the radial velocity is from Karachentsev & Kashibadze (2006).[6] The equatorial proper motion, radial velocity, and coordinates were transformed into the heliocentric galactic Cartesian system using the `astropy.coordinates` package. X is directed to the MW center, Y is directed along the solar rotational motion within the MW plane, and Z is directed toward the MW north pole so that XYZ is a right-handed system. By adding the solar velocity and subtracting the MW center coordinates, taken as (9.5, 250.7, 8.56) km s^{-1} and (8.249, 0, −0.0208) kpc from Akhmetov et al. 2024 (and references therein), we obtained the galactocentric coordinates and velocities within the reference system, which we refer to as XYZ.

Next, as the two-body problem can be simplified to two dimensions, we will use the XYZ transformation to limit our consideration of all possible orbits for And XVIII to those that lie in the new $X'''Y'''$ plane (the aforementioned plane defined by the MW, M31, and And XVIII). To realize this, we applied first the rotation for ϕ_1 with $Z = Z'$, second the rotation for ϕ_2 with $X' = X''$, and third the rotation with ϕ_3 and $Y'' = Y'''$, where the rotation is counterclockwise. The A18 subscripts in the equations below are for And XVIII's values. The applied angles are as follows:

$$\phi_1 = \arctan\left(\frac{Y_{A18}}{X_{A18}}\right) - \frac{\pi}{2}; \quad \phi_2 = \arctan\left(\frac{Z_{A18}}{\sqrt{X_{A18}^2 + Y_{A18}^2}}\right);$$
$$\phi_3 = 3\pi - \arctan\left(\frac{Z''_{M31}}{X''_{M31}}\right), \tag{A1}$$

with *arctan* derived between 0 and 2π, where

$$\begin{bmatrix} X'' \\ Y'' \\ Z'' \end{bmatrix} = \begin{bmatrix} 1 & 0 & 0 \\ 0 & \cos(\phi_2) & \sin(\phi_2) \\ 0 & -\sin(\phi_2) & \cos(\phi_2) \end{bmatrix} \begin{bmatrix} \cos(\phi_1) & \sin(\phi_1) & 0 \\ -\sin(\phi_1) & \cos(\phi_1) & 0 \\ 0 & 0 & 1 \end{bmatrix} \begin{bmatrix} X \\ Y \\ Z \end{bmatrix}, \tag{A2}$$

which gives

$$Z''_{M31} = \sin(\phi_2)\sin(\phi_1)X_{M31} - \sin(\phi_2)\cos(\phi_1)Y_{M31} + \cos(\phi_2)Z_{M31};$$
$$X''_{M31} = \cos(\phi_1)X_{M31} + \sin(\phi_1)Y_{M31}. \tag{A3}$$

The overall transformation looks like:

$$\begin{bmatrix} X''' \\ Y''' \\ Z''' \end{bmatrix} = \begin{bmatrix} \cos(\phi_3) & 0 & -\sin(\phi_3) \\ 0 & 1 & 0 \\ \sin(\phi_3) & 0 & \cos(\phi_3) \end{bmatrix} \begin{bmatrix} 1 & 0 & 0 \\ 0 & \cos(\phi_2) & \sin(\phi_2) \\ 0 & -\sin(\phi_2) & \cos(\phi_2) \end{bmatrix} \times \begin{bmatrix} \cos(\phi_1) & \sin(\phi_1) & 0 \\ -\sin(\phi_1) & \cos(\phi_1) & 0 \\ 0 & 0 & 1 \end{bmatrix} \begin{bmatrix} X \\ Y \\ Z \end{bmatrix}. \tag{A4}$$

The obtained transformation aligns the Y''' axis with the line that passes through the MW center and And XVIII, and it sets the plane determined by the MW center, M31, and And XVIII to be coincident with $X'''Y'''$ plane. The new coordinate system center is at the MW center (i.e., only rotations were applied).

The obtained transformation is constrained in equatorial coordinates by the known radial velocity of And XVIII (−337.2 km s^{-1}) and by our requirement that $W'''_{A18} - W'''_{M31} = 0$ km s^{-1} in the new coordinate system. Figure 11 (left) is color-coded by the $W'''_{A18} - W'''_{M31}$ values, and the orange line indicates $W'''_{A18} - W'''_{M31} = 0$ km s^{-1}. The colored circles illustrate the

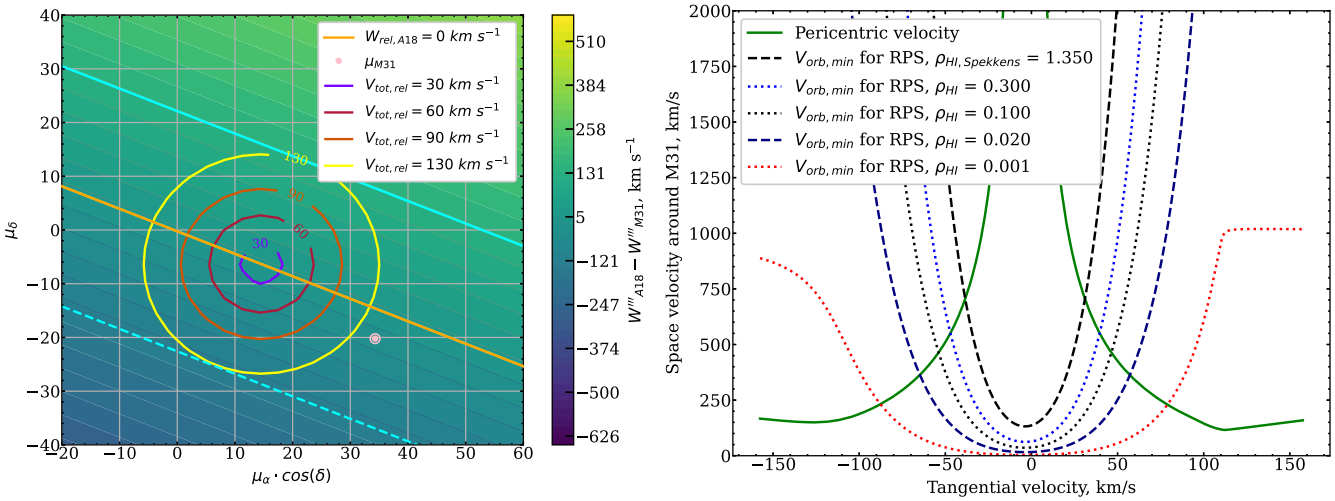

Figure 11. Left: Possible $W'''_{A18} - W'''_{M31}$ values for a selected range of $\mu_\alpha \cos(\delta)$, μ_δ (in μas yr^{-1}). The orange line is for $W'''_{A18} - W'''_{M31} = 0$, and the blue lines are for 130 km s^{-1}. The circles show And XVIII's total velocity relative to M31. These regions are overlapping with the $V'''_{A18} - V'''_{M31}$ values from Sections C and D. The pink point shows the adopted proper motion of M31 (van der Marel et al. 2012b). Right: Pericentric velocity and lowest orbital velocity for various hydrogen densities, based on the ram pressure stripping condition from Gunn et al. (1972) (Section B). For absolute values of relative tangential velocities (see Section A), if the velocity is larger than 31–38 km s^{-1}, the pericentric distance will be far enough and the pericentric velocity will be small enough for And XVIII *not* to have experienced the RPS in the past. Therefore, RPS is ineffective where the green curve lies below the RPS curve for the various hydrogen densities. The M31 halo and And XVIII ISM gas densities are in cm^{-3}.

[6] The M31 center coordinates were taken from https://esahubble.org/images/opo1204b/.

absolute values of And XVIII's velocity relative to M31. For the part of the orange line on the diagram within the circles, $V'''_{A18} - V'''_{M31}$, the projection of And XVIII's relative velocity toward the MW center will be $-18.4 \pm 0.4\,\mathrm{km\,s^{-1}}$. The nonconstancy of the relative radial velocity ($V'''_{A18} - V'''_{M31}$) for different proper motions, for which $W'''_{A18} - W'''_{M31} = 0$, is the motivation for transforming from equatorial coordinates to a new coordinate system. However, the relative tangential component of $|U'''_{A18} - U'''_{M31}| \lesssim 150\ \mathrm{km\,s^{-1}}$, which causes And XVIII to be bound to M31, also makes the variation in $V'''_{A18} - V'''_{M31}$ small ($\pm 0.4\,\mathrm{km\,s^{-1}}$). Therefore, we will consider the relative radial velocity of And XVIII as a constant in our discussion.

To summarize, we take And XVIII's v_r velocity to be $V'''_{A18} - V'''_{M31} = -18.4\,\mathrm{km\,s^{-1}}$. Here, v_τ (And XVIII's tangential velocity relative to M31) is equal to $U'''_{A18} - U'''_{M31}$. We use the subscript 0 to assign And XVIII's orbital parameters relative to M31 at the present time. In these appendices, the terms "relative line-of-sight velocity" and "relative radial velocity" are projected onto the line connecting the MW center to And XVIII, not the line connecting the Sun to And XVIII. Thus, v_{r0} and $v_{\tau 0}$ are defined as And XVIII's radial and transverse velocities relative to the MW center at the current time, and the following equations describe And XVIII's velocity relative to M31:

$$U'''_{A18} - U'''_{M31} = v_{\tau 0}; \quad V'''_{A18} - V'''_{M31} = v_{r0} = -18.4\ km\ s^{-1}; \quad W'''_{A18} - W'''_{M31} = 0\ km\ s^{-1}. \tag{A5}$$

Appendix B
RPS after M31 Halo Passage

We consider whether M31 could have gradually tidally stripped And XVIII without engaging in rapid RPS. In this scenario, the gas loss could be gradual enough to allow for the extended SFH observed by Makarova et al. (2017).

From Spekkens et al. (2014) (and references therein, including Gunn et al. 1972), the condition for RPS is

$$\rho_{\mathrm{M31}} v_{\mathrm{orb}}^2 > 5 \rho_{\mathrm{dw}} \sigma_{\mathrm{dw}}^2, \tag{B1}$$

where ρ_{M31} is the gas density of the host galaxy halo, v_{orb} is the dwarf galaxy's orbital velocity at the corresponding ρ_{M31}, ρ_{dw} is the ISM gas density of the dwarf galaxy, and σ_{dw} is the velocity dispersion of the dwarf galaxy's stars.

If we expect And XVIII to be bound to M31 and to be gradually tidally stripped, but not ram pressure stripped, its pericentric velocity should be low enough (Figure 11, right). For the two-body problem (Appendix C), the pericentric velocity depends on the unknown current tangential velocity relative to M31, but the hydrogen density in M31's halo will also depend on the pericentric distance. The particle density may be comparable with a hot electron density within a halo, taken from Tahir et al. (2022) as

$$n_e^{\mathrm{H}}(r) = \frac{n_0^{\mathrm{H}}}{\mu_e (r/r_c + 0.75)(r/r_c + 1)^2}, \tag{B2}$$

where $n_0^{\mathrm{H}} = 3.4 \times 10^{-2}\,\mathrm{cm^{-3}}$, $r_c = 15\,\mathrm{kpc}$, and $\mu_e = 1.18$. Taken all together, the constraints on the relative tangential velocity of And XVIII that make it bound with M31 (details in Appendix C) and shielded from complete ram pressure stripping (with the dSph gas density at its maximum possible value, $1.35\,\mathrm{cm^{-3}}$, Spekkens et al. 2014) are about

$$31\ \mathrm{km\,s^{-1}} < v_{\tau 0} < 157.6\ \mathrm{km\,s^{-1}}. \tag{B3}$$

Appendix C
Two-body Problem

We consider the orbit of And XVIII around M31, assuming a point-like, static potential for both galaxies. The results are illustrated in Figure 12. In Appendix D, we extend the model to include the MW.

We used $M_{\mathrm{M31}} = 1.69 \times 10^{12}\,M_\odot$, $M_{\mathrm{MW}} = 1.5 \times 10^{12}\,M_\odot$, $v_{r,\mathrm{M31}} = -301\,\mathrm{km\,s^{-1}}$, $v_{r,\mathrm{AndXVIII}} = -337.2\,\mathrm{km\,s^{-1}}$, $r_0 = 579\,\mathrm{kpc}$ as the 3D distance from And XVIII to M31, and $r_p = 113.6\,\mathrm{kpc}$ as the projected distance between M31 and And XVIII (the absolute value of the X''' coordinate of the M31; see our Appendix A, Makarova et al. (2017), van der Marel et al. (2012b), and Karachentsev & Kashibadze (2006)). The orbit is assumed to lie in the plane defined by the MW center—And XVIII line and M31's position, so $v_{r0} \approx -18.4\,\mathrm{km\,s^{-1}}$ (see Section A).

For the pericentric and apocentric positions, the distances and velocities can be found from energy and angular momentum conservation laws written as

$$\frac{(v_{r0}^2 + v_{\tau 0}^2)}{2} - \frac{GM_{\mathrm{M31}}}{r_0} = \frac{v^2}{2} - \frac{GM_{\mathrm{M31}}}{r}$$
$$r_0 \left[-v_{r0} \sin\left(\frac{r_p}{r_0}\right) + v_{\tau 0} \cos\left(\frac{r_p}{r_0}\right) \right] = rv. \tag{C1}$$

The equations for distance and velocity at pericenter (+) and apocenter (−) can be obtained from

$$r_\pm = \frac{-1 \pm \sqrt{1 + 4[(-v_{r0} \sin(r_p/r_0) + v_{\tau 0} \cos(r_p/r_0))^2\, r_0/(2GM_{\mathrm{M31}})][(v_{r0}^2 + v_{\tau 0}^2) r_0/(2GM_{\mathrm{M31}}) - 1]}}{(2/r_0)[(v_{r0}^2 + v_{\tau 0}^2) r_0/(2GM_{\mathrm{M31}}) - 1]} \tag{C2}$$

$$v_\pm = \frac{r_0}{r_\pm} \left(-v_{r0} \sin\left(\frac{r_p}{r_0}\right) + v_{\tau 0} \cos\left(\frac{r_p}{r_0}\right) \right). \tag{C3}$$

The upper limit for the unknown transverse velocity relative to M31 is obtained from the equality of energy to 0, which is around $157.6\,\mathrm{km\,s^{-1}}$. The apocentric and pericentric distances for zero tangential velocity will be about 586.4 kpc and 0.3 kpc, respectively, with orbital velocities about 3.6 and $6975\,\mathrm{km\,s^{-1}}$. Necessarily, this would mean that And XVIII lost all its gas due to ram pressure stripping (and tidal destruction).

Now we can consider the time since the last pericentric passage (Figure 12). The eccentricity dependence on the unknown tangential velocity is

$$e = \sqrt{1 + 4\left[-v_{r0} \sin\left(\frac{r_p}{r_0}\right) + v_{\tau 0} \cos\left(\frac{r_p}{r_0}\right) \right]^2 \frac{r_0}{2GM_{M31}} \left[\frac{(v_{r0}^2 + v_{\tau 0}^2) r_0}{2GM_{M31}} - 1 \right]}. \tag{C4}$$

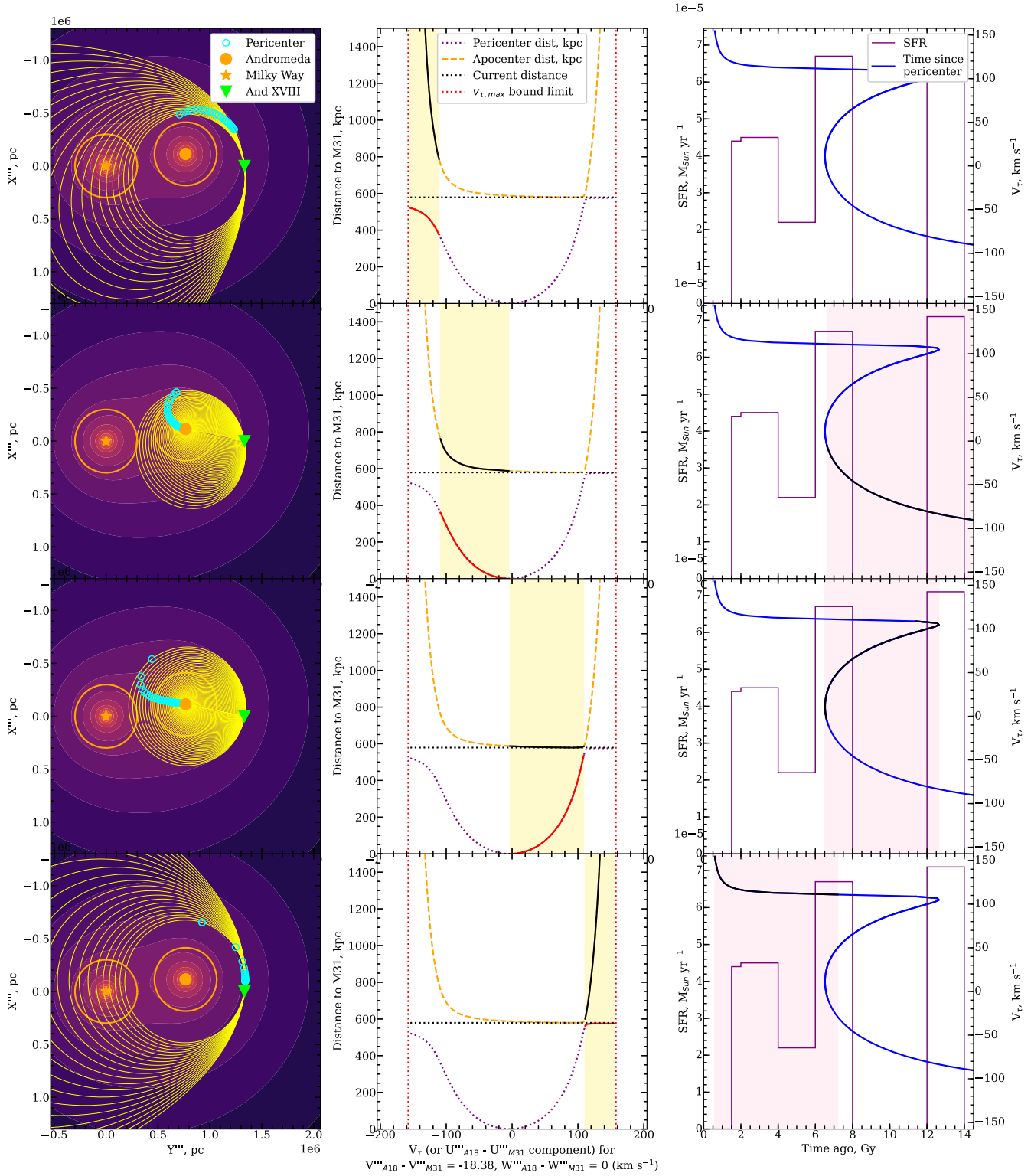

Figure 12. Left*:* And XVIII's expected orbits for different tangential velocities. The transverse motion is positive for the downward direction. The colored background of MW and M31 gravitational potential is shown for the reference and was not used for this modeling. The different yellow orbits correspond to the different assumed tangential velocities, shadowed in the middle and right panels (not for different times). Middle column: Distances from M31 for varying values of $v_{\tau 0}$. Right*:* SFR (Makarova et al. 2017) and tangential velocity ($v_{\tau 0}$) vs. time since the last pericentric passage. The "upper" branch of the time of pericentric flyby (right panels) precludes RPS because those pericentric distances are outside of the virial radius of M31, illustrated by cyan in the left panels. The second and the third rows give the region where RPS is possible. The first and the last rows include orbits that intercept the virial radius of the MW. For these situations, the two-body problem is insufficient (see Appendix D).

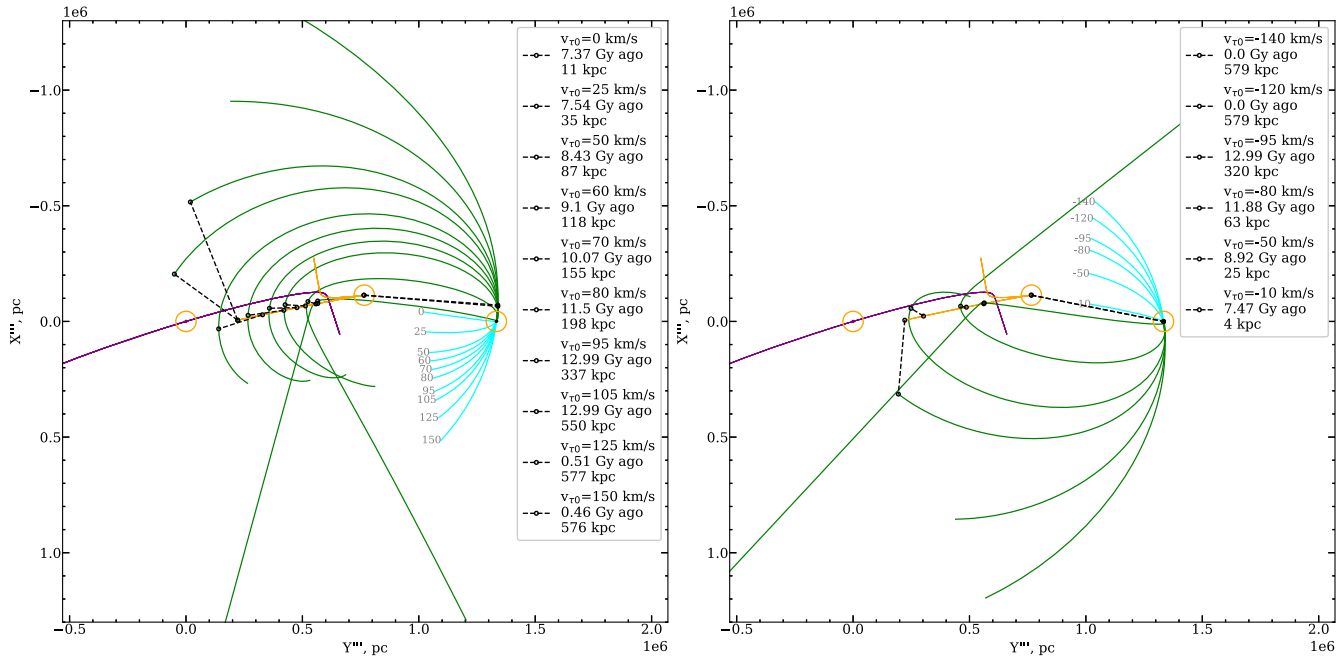

Figure 13. Left*:* Three-body modeling for assumed $v_{\tau 0}$ of And XVIII relative to M31 as a positive value (clockwise). Right*:* The same for the negative relative to M31 tangential velocities (counterclockwise). Green color is for the past motion of And XVIII (up to 13 Gy ago); blue is for future motion (up to 3.86 Gy, before the expected M31–MW interaction; van der Marel et al. 2012a); orange is for M31 motion, with orange circles for current M31, MW ,and And XVIII positions; purple is for MW motion; and black dashed segments indicate the shortest lines between And XVIII and M31, with $v_{\tau 0}$, time of passage, and the distance as assigned in the plot's legend.

The positional angle (θ) is substituted into the time integral for this problem as

$$\tan\frac{\theta_0}{2} = \sqrt{\frac{1+e}{1-e}}\tan\frac{\psi_0}{2} \tag{C5}$$

$$r_0 = a(1 - e\cos\psi_0) \tag{C6}$$

$$\tan\frac{\psi_0}{2} = \sqrt{2\left[\frac{1}{e}\left(1 - \frac{r_0}{a}\right) + 1\right]^{-1} - 1} \tag{C7}$$

$$t_0 = \frac{[r_0[-v_{r0}\sin(r_p/r_0) + v_{\tau 0}\cos(r_p/r_0)]]^3}{[GM_{M31}]^2} \times \int_0^{\theta_0}\frac{d\theta}{(1+e\cos\theta)^2}, \tag{C8}$$

where r_0 is the current distance from And XVIII to M31, θ_0 is the current position angle of And XVIII on its orbit, and ψ_0 is the current eccentric position angle of And XVIII. The integration starts from 0, the position angle of the pericenter.

We considered the tangential velocity of And XVIII in both directions within the M31—And XVIII plane. The reader may compare Figure 12 (the first and the last rows) with Figure 13.

To summarize the results illustrated in Figure 12, a natural limit on the pericentric distance to experience RPS can be related to the range of relative tangential velocity that leads to a semimajor axis smaller than the And XVIII's current distance to M31: $|v_{\tau 0}| < 110.5$ km s^{-1}. This situation is shown in the second and third rows of Figure 12, where the pericentric points (cyan) are preferentially inside the virial radius of M31.

Appendix D
Three-body Problem

We show some of And XVIII's possible orbits in the three-body problem including And XVIII, M31, and the MW (Figure 13).[7] The time step is 0.01 Gy. We assumed static, point-like potentials for each galaxy, and we ignored cosmological expansion. The variables are defined within the reference system shown in Figure 13, with the MW at the center at the current time ($z = 0$). M31's current velocity is defined to be 0, and we adopted the velocity of the MW relative to M31 as M31's velocity with the opposite sign (described in Appendix A). And XVIII's mass was assigned as $10^{7.38}\,M_\odot$ (Table 4).

Both panels of Figure 13 are in accordance with Figure 12, although the $X'''Z'''$, $Y'''Z'''$ projections have not been described here.

The closest distances from And XVIII to M31 (black dashed lines in Figure 13) show that the upper limit on $v_{\tau 0}$ to experience RPS is about 80 km s^{-1} for the positive direction (left panel) and about -90 km s^{-1} for the negative direction (right panel). These tangential velocities correspond to pericentric distances of $r_{\rm min} > r_{\rm vir,M31} \approx 200$ kpc (Gilbert et al. 2012; Tollerud et al. 2012) for $|v_{\tau 0}| > 80$ (90) km s^{-1}. These numbers seems to agree with our findings from the two-body problem (Appendix C).

Our conclusions about the backsplash hypothesis, considering the three-body problem, are as follows:

1. And XVIII cannot be a renegade dwarf galaxy. If it is a backsplash dSph, it passed near M31, not the MW.

[7] https://github.com/blbadger/threebody

2. It is possible to consider proper motion in both the clockwise and counterclockwise directions in the LOS–M31 plane. RPS is possible in either scenario.
3. The two-body problem seems to be sufficient here because the MW is a minor influencer of And XVIII's orbit. In other words, the tangential velocity limits derived in Section C can be applied to all possible orbit inclinations, not only for the plane of motion as defined in Appendix A.

ORCID iDs

Kateryna A. Kvasova https://orcid.org/0000-0002-7438-1059
Evan N. Kirby https://orcid.org/0000-0001-6196-5162
Rachael L. Beaton https://orcid.org/0000-0002-1691-8217

References

Akaike, H. 1974, ITAC, 19, 716
Akhmetov, V. S., Bucciarelli, B., Crosta, M., et al. 2024, MNRAS, 530, 710
Arimoto, N., & Yoshii, Y. 1987, A&A, 173, 23
Astropy Collaboration, Robitaille, T. P., Tollerud, E. J., et al. 2013, A&A, 558, A33
Astropy Collaboration, Price-Whelan, A. M., Sipőcz, B. M., et al. 2018, AJ, 156, 123
Astropy Collaboration, Price-Whelan, A. M., Lim, P. L., et al. 2022, ApJ, 935, 167
Battaglia, G., Irwin, M., Tolstoy, E., et al. 2008, MNRAS, 383, 183
Beaton, R. L. 2014, PhD thesis, Univ. Virginia
Benavides, J. A., Sales, L. V., Abadi, M. G., et al. 2021, NatAs, 5, 1255
Benítez-Llambay, A., Navarro, J. F., Abadi, M. G., et al. 2016, MNRAS, 456, 1185
Bennet, P., Sand, D. J., Zaritsky, D., et al. 2018, ApJL, 866, L11
Bermejo-Climent, J. R., Battaglia, G., Gallart, C., et al. 2018, MNRAS, 479, 1514
Boyer, M. L., McQuinn, K. B. W., Barmby, P., et al. 2015, ApJS, 216, 10
Canterna, R. 1976, AJ, 81, 228
Cardona-Barrero, S., Battaglia, G., Di Cintio, A., Revaz, Y., & Jablonka, P. 2021, MNRAS: Lett., 505, L100
Collins, M. L. M., Chapman, S. C., Rich, R. M., et al. 2013, ApJ, 768, 172
Conn, A. R., Ibata, R. A., Lewis, G. F., et al. 2012, ApJ, 758, 11
Cooper, M. C., Newman, J. A., Davis, M., Finkbeiner, D. P., & Gerke, B. F., 2012 spec2d: DEEP2 DEIMOS Spectral Pipeline, Astrophysics Source Code Library, ascl:1203.003
Danieli, S., van Dokkum, P., Conroy, C., Abrahem, R., & Romanowsky, A. J. 2019, ApJL, 874, L12
DESI Collaboration, Adame, A. G., Aguilar, J., et al. 2024, arXiv:2404.03002
Di Cintio, A., Mostoghiu, R., Knebe, A., & Navarro, J. F. 2021, MNRAS, 506, 531
Dolphin, A., 2016 DOLPHOT: Stellar photometry, Astrophysics Source Code Library, ascl:1608.013
D'Onghia, E., Besla, G., Cox, T. J., & Hernquist, L. 2009, Natur, 460, 605
Drlica-Wagner, A., Bechtol, K., Mau, S., et al. 2020, ApJ, 893, 47
Escala, I., Kirby, E. N., Gilbert, K. M., Cunningham, E. C., & Wojno, J. 2019, ApJ, 878, 42
Faber, S. M., Phillips, A. C., Kibrick, R. I., et al. 2003, Proc. SPIE, 4841, 1657
Foreman-Mackey, D. 2016, JOSS, 1, 24
Foreman-Mackey, D., Hogg, D. W., Lang, D., & Goodman, J. 2013, PASP, 125, 306
Geisler, D. 1996, AJ, 111, 480
Genina, A., Frenk, C. S., Benítez-Llambay, A., et al. 2019, MNRAS, 488, 2312
Gilbert, K. M., Guhathakurta, P., Kalirai, J. S., et al. 2006, ApJ, 652, 1188
Gilbert, K. M., Guhathakurta, P., Beaton, R. L., et al. 2012, ApJ, 760, 76
Girardi, L., Bertalli, G., Bressan, A., et al. 2002, A&A, 391, 195
Goldman, S. R., Boyer, M. L., McQuinn, K. B. W., et al. 2019, ApJ, 877, 49
Goodman, J., & Weare, J. 2010, CAMCS, 5, 65
Gunn, J. E., Gott, J., & Richard, I. 1972, ApJ, 176, 1
Higgs, C. R., & McConnachie, A. W. 2021, MNRAS, 506, 2766
Hunter, J. D. 2007, CSE, 9, 90
Ibata, R. A., Lewis, G. F., McConnachie, A. W., et al. 2014, ApJ, 780, 128
Karachentsev, I. D., & Kashibadze, O. 2006, Ap, 49, 3
Kirby, E. N. 2011, PASP, 123, 531
Kirby, E. N., Cohen, J. G., Guhathakurta, P., et al. 2013, ApJ, 779, 102
Kirby, E. N., Guhathakurta, P., Bolte, M., Sneden, C., & Geha, M. C. 2009, ApJ, 705, 328
Kirby, E. N., Guhathakurta, P., & Sneden, C. 2008, ApJ, 682, 1217
Kirby, E. N., Lanfranchi, G. A., Simon, J. D., Cohen, J. G., & Guhathakurta, P. 2011, ApJ, 727, 78
Kirby, E. N., Simon, J. D., & Cohen, J. G. 2015a, ApJ, 810, 56
Kirby, E. N., Guhathakurta, P., Simon, J. D., et al. 2010, ApJS, 191, 352
Kirby, E. N., Guo, M., Zhang, A. J., et al. 2015b, ApJ, 801, 125
Knebe, A., Libeskind, N. I., Doumler, T., et al. 2011, MNRAS, 417, L56
Kurucz, R. L., 2017 ATLAS9: Model atmosphere program with opacity distribution functions, Astrophysics Source Code Library, ascl:1710.017
Landolt, A. U. 1992, AJ, 104, 340
Leaman, R., Venn, K. A., Brooks, A. M., et al. 2013, ApJ, 767, 131
Lelli, F., Verheijen, M., & Fraternali, F. 2014, MNRAS, 445, 1694
Li, H., Hammer, F., Babusiaux, C., et al. 2021, ApJ, 916, 8
Libralato, M., Bellini, A., van der Marel, R. P., et al. 2023, ApJ, 950, 101
Majewski, S. R., Ostheimer, J. C., Kunkel, W. E., & Patterson, R. J. 2000, AJ, 120, 2550
Majewski, S. R., Beaton, R. L., Patterson, R. J., et al. 2007, ApJL, 670, L9
Makarova, L. N., Makarov, D. I., Karachentsev, I. D., Tully, R. B., & Rizzi, L. 2017, MNRAS, 464, 2281
McConnachie, A., Huxor, A., Martin, N., et al. 2008, ApJ, 688, 1009
McConnachie, A. W. 2012, AJ, 144, 4
McConnachie, A. W., Ibata, R., Martin, N., et al. 2018, ApJ, 868, 55
Miyoshi, T., & Chiba, M. 2020, ApJ, 905, 109
Monet, D. G., Levine, S. E., Canzian, B., et al. 2003, AJ, 125, 984
Newman, J. A., Cooper, M. C., Davis, M., et al. 2013, ApJS, 208, 5
Ostheimer, J., & Craig, J. 2003, PhD thesis, Univ. Virginia
Simon, J. D. 2018, ApJ, 863, 89
Simon, J. D., & Geha, M. 2007, ApJ, 670, 313
Sneden, C., Bean, J., Ivans, I., Lucatello, S., & Sobeck, J., 2012 MOOG: LTE line analysis and spectrum synthesis, Astrophysics Source Code Library, ascl:1202.009
Sneden, C. A. 1973, PhD thesis, Univ. Texas, Austin
Sohn, S. T., Majewski, S. R., Muñoz, R. R., et al. 2007, ApJ, 663, 960
Spekkens, K., Urbancic, N., Masob, B. S., Willman, B., & Aguirre, J. E. 2014, ApJL, 795, L5
Starkenburg, E., Hill, V., Tolstoy, E., et al. 2010, A&A, 513, A34
Stetson, P. B. 1987, PASP, 99, 191
Stetson, P. B. 1990, PASP, 102, 932
Stetson, P. B. 1994, PASP, 106, 250
Sugiura, N. 1978, Commun. Stat. Theory Methods, 7, 13
Tahir, N., De Paolis, F., Qadir, A., & Nucita, A. A. 2022, A&A, 664, A30
Taibi, S., Battaglia, G., Leaman, R., et al. 2022, A&A, 665, A92
Teyssier, M., Johnston, K. V., & Kuhlen, M. 2012, MNRAS, 426, 1808
Tollerud, E. J., Beaton, R. L., Geha, M. C., et al. 2012, ApJ, 752, 45
van der Marel, R. P., Besla, G., Cox, T. J., Sohn, S. T., & Anderson, J. 2012a, ApJ, 753, 9
van der Marel, R. P., Fardal, M., Besla, G., et al. 2012b, ApJ, 753, 8
van der Walt, S., Colbert, S. C., & Varoquaux, G. 2011, CSE, 13, 22
Virtanen, P., Gommers, R., Oliphant, T. E., et al. 2020, NatMe, 17, 261
Walker, M. G., & Peñarrubia, J. 2011, ApJ, 742, 20
Weisz, D. R., Dalcanton, J. J., Williams, B. F., et al. 2011, ApJ, 739, 5
Weisz, D. R., Martin, N. F., Dolphin, A. E., et al. 2019, ApJL, 885, L8
Wojno, J., Gilbert, K. M., Kirby, E. N., et al. 2020, ApJ, 895, 78
Wolf, J., Martinez, G. D., Bullock, J. S., et al. 2010, MNRAS, 406, 1220